INTERNATIONAL JOURNAL FOR NUMERICAL METHODS IN FLUIDS
Int. J. Numer. Meth. Fluids 2001; **37**: 797–835 (DOI: 10.1002/fld.179)

High-order filtering for control volume flow simulation

G. De Stefano, F. M. Denaro*,[1] and G. Riccardi

Dipartimento di Ingegneria Aerospaziale, Seconda Universitá di Napoli, Aversa, Italy

SUMMARY

A general methodology is presented in order to obtain a hierarchy of high-order filter functions, starting from the standard top-hat filter, naturally linked to control volumes flow simulations. The goal is to have a new filtered variable better represented in its high resolved wavenumber components by using a suitable deconvolution. The proposed formulation is applied to the integral momentum equation, that is the evolution equation for the top-hat filtered variable, by performing a spatial reconstruction based on the approximate inversion of the averaging operator. A theoretical analysis for the Burgers' model equation is presented, demonstrating that the local de-averaging is an effective tool to obtain a higher-order accuracy. It is also shown that the subgrid-scale term, to be modeled in the deconvolved balance equation, has a smaller absolute importance in the resolved wavenumber range for increasing deconvolution order. A numerical analysis of the procedure is presented, based on high-order upwind and central fluxes reconstruction, leading to congruent control volume schemes. Finally, the features of the present high-order conservative formulation are tested in the numerical simulation of a sample turbulent flow: the flow behind a backward-facing step. Copyright © 2001 John Wiley & Sons, Ltd.

KEY WORDS: approximate deconvolution; control volume approach; high-order filtering; large-eddy simulation

1. INTRODUCTION

Numerical simulation of turbulent flows requires a careful treatment of the transport equations, generally dealt with in filtering procedures. In fact, due to the difficulties in performing direct numerical simulation (DNS) over the entire range of turbulent scales, the adoption of filtering approaches is the only possibility for resolving problems of practical interest. Modern filtering approaches, such as large-eddy simulation (LES), are based on a formal separation between large (resolved) and small (unresolved) scales, obtained by truncating high frequency solution components. Despite this formal separation, as a consequence of the non-linearity of the governing equations, subgrid scales (SGS) models are required to take into account the effects of the unresolved field on the resolved one.

* Correspondence to: Dipartimento di Ingegneria Aerospaziale, Seconda Universitá di Napoli, via Roma 29, 81031 Aversa (Ce), Italy.
[1] E-mail: denaro@unina.it

Received May 1999
Revised December 2000

Among different ways to filter the transport equations, spatial filtering is one of the most common. In this method, the flow variables are smoothed by eliminating wavelengths not resolvable on a given grid. A spatial filtering can result both from explicit pre-filtering (e.g. a volume integration) and from implicit filtering, introduced by finite differences (FD) discretization of the equations. Formulations rising from this procedure were adopted in the past years (e.g. see References [1,2]) by applying the so-called top-hat filter. Recently, many authors [3–5] have highlighted that the theoretical analysis of an SGS model and its practical implementation should be jointly considered. Indeed, filtering effects and numerical errors could be responsible for misleading results, even if theoretically efficient models were adopted.

Previously, we presented a high-order control volumes (CVs) approach for solving unsteady Navier–Stokes equations and some preliminary results were obtained for moderately high Reynolds number flows [6–8]. In the present paper, we formalize and apply an extension of that approach in the framework of a high-order filtering formulation for LES of turbulent flows.

The procedure is based on the approximate deconvolution of the top-hat filtered equations, allowing us to define a class of high-order filtered variables, according to the formal order of the field reconstruction. As will be shown, by increasing the de-averaging order, the modified filter tends towards the spectral cut-off, which results more appealing from the LES point of view [9] because the SGS stresses account only for the effects of the small scales on the large ones. On the contrary, smooth filters (e.g. the top-hat one) get no sharp separation between the flow scales and the physical meaning of the filtered velocity appears less clear. However, sharp cut-off filtering is naturally related to spectral methods, which are limited to simulations of flows in simple geometries.

The aim of this paper is to introduce a high-order filtering for CV methods that are applicable to more general problems than spectral ones. After introducing the averaging differential operator and its approximate inverse one, we derive an evolution equation for the deconvolved variable by applying the inverse operator to each term of the momentum equation. A theoretical analysis is presented and the effects of high-order filtering for LES are addressed. An SGS similarity model naturally linked to the actual filter is also examined.

As a matter of fact, since the pioneering work by Leonard [10], many authors have exploited the deconvolution approach for an approximate evaluation of the SGS stresses in the LES equations, but leaving unaltered the resolved top-hat filtered variable [11–14]. The present approach is substantially different as we solve LES equations directly for the deconvolved variable. The possibility of interpreting the inverse modeling in terms of the solution of an evolution equation for the deconvolved variable was briefly addressed in a letter [13].

Our analysis is completed by considering some spatial discretizations consistent with the introduced high-order filtering procedure. It will be shown that the coherent application of our procedure allows us to develop high-order conservative schemes, which can be considered for LES. In order to explore the effective performances of such schemes, we present and compare upwind- and central-flux reconstruction for the discretization of the convective term in one dimension. As a matter of fact, upwind schemes are considered inappropriate for LES, since derivatives discretized over non-symmetric supports present modified wavenumbers having a non-vanishing imaginary part. Thus, upwind schemes introduce a dissipative numerical error, acting mainly at high resolved wavenumbers, which can contaminate the modeled SGS stress

[15,16]. On the other hand, the simulation of wall-bounded flows requires the adoption of non-uniform grids, for which central schemes involve dissipation errors, too.

As an example, the present numerical procedure is applied (up to the second-order accuracy) in the simulation of a real turbulent flow: the vorticity shedding behind a backward-facing step (BFS). Flow statistics are reported and the vortex visualization is carried out by identifying the main vortical structures in the flow, defined according to the criterion introduced in Jeong and Hussain [17].

The outline of the paper is as follows: Section 2 is devoted to the introduction of the reconstruction procedure and the definition of the inverse operator which will be applied in order to deconvolve the volume averaged Navier–Stokes equations. In Section 3, a theoretical analysis is presented for the one-dimensional case and the high-order filter is applied to the Burgers' model equation. The actual numerical implementation of the procedure is examined in Section 4, while the results of the simulation of the BFS turbulent flow are presented in Section 5. Finally, some conclusions are addressed in Section 6.

2. A LOCAL AVERAGE-BASED PROCEDURE FOR TRANSPORT EQUATIONS IN CONSERVATIVE FORM

In this section the formulation is derived within the general framework of three-dimensional flow of an incompressible fluid, described by the solution of the Navier–Stokes equations. These are written in conservative form

$$\frac{\partial u_i}{\partial t} = \frac{\partial f_{ik}}{\partial x_k} \tag{1}$$

where $f_{ij} = -u_i u_j - \delta_{ij} p/\rho_0 + \nu\, \partial u_i/\partial x_j$, δ_{ij} being the Kronecker symbol, ρ_0 the constant density and ν the kinematic viscosity of the fluid. Equation (1) is solved in a domain D, associated with the divergence-free velocity constraint $\partial u_i/\partial x_i = 0$ and proper boundary conditions.

In the LES of turbulent flows, the velocity field is often spatially filtered according to (time dependence is omitted)

$$\bar{u}_i(\boldsymbol{x}) = \frac{1}{|\Omega|} \int_{\Omega(\boldsymbol{x})} \mathrm{d}\boldsymbol{x}' u_i(\boldsymbol{x}') \tag{2}$$

where $\Omega(\boldsymbol{x}) \subset D$ is a control volume. The integral balance equation for the ith velocity component results

$$\frac{\partial \bar{u}_i}{\partial t} = \frac{1}{|\Omega|} \int_{\partial\Omega} \mathrm{d}S\, n_k f_{ik} \tag{3}$$

where if $\Omega(\boldsymbol{x}) = \boldsymbol{x} + \Omega(\boldsymbol{0})$, averaging and spatial differentiating commute [18] so that, in local form, one gets

$$\frac{\partial \bar{u}_i}{\partial t} = \frac{\partial \bar{f}_{ik}}{\partial x_k} \tag{4}$$

After partitioning the domain D in CVs fixed in space, the volume balance procedure expressed by (4) was adopted by Schumann [2], by using a discretization of the field in terms of piece-wise constant functions. In the present approach, as in Deardorff [1], the averaged velocity is a continuous function in space. By using an m-th order Taylor expansion for u_i in Equation (2), one obtains the filtered field in terms of the unfiltered one

$$\bar{u}_i(\boldsymbol{x}) \cong u_i(\boldsymbol{x}) + \sum_{l=1}^{m} \frac{1}{l!} \sum_{l_1+l_2+l_3=l} c_{l_1,l_2,l_3}(\boldsymbol{x}) D_{\boldsymbol{x}}^{(l_1,l_2,l_3)} u_i$$

where $D_{\boldsymbol{x}}^{(l_1,l_2,l_3)} = \partial_{x_1}^{l_1} \partial_{x_2}^{l_2} \partial_{x_3}^{l_3}$ represents a lth order three-dimensional derivative and the coefficients in the sum are given by the moments of the top-hat filter function

$$c_{l_1,l_2,l_3}(\boldsymbol{x}) = \frac{1}{|\Omega|} \int_{\Omega(\boldsymbol{x})} \mathrm{d}\boldsymbol{x}' \prod_{k=1}^{3} (x_k' - x_k)^{l_k} \tag{5}$$

For hexaedrical CVs of given size, these coefficients are constant so that, by introducing the linear differential operator of mth accuracy order

$$R_{\boldsymbol{x}}^{(m)} = -\sum_{l=1}^{m} \frac{1}{l!} \sum_{l_1+l_2+l_3=l} c_{l_1,l_2,l_3} D_{\boldsymbol{x}}^{(l_1,l_2,l_3)} \tag{6}$$

the top-hat filtered velocity can be approximated as

$$\bar{u}_i(\boldsymbol{x}) \cong [I_{\boldsymbol{x}} - R_{\boldsymbol{x}}^{(m)}] u_i$$

with $I_{\boldsymbol{x}}$ the identity at $\boldsymbol{x}$. As will be shown in the following, the averaging operator $I_{\boldsymbol{x}} - R_{\boldsymbol{x}}^{(m)}$ can be inverted according to the following expansion

$$[I_{\boldsymbol{x}} - R_{\boldsymbol{x}}^{(m)}]^{-1} = I_{\boldsymbol{x}} + R_{\boldsymbol{x}}^{(m)} + [R_{\boldsymbol{x}}^{(m)}]^2 + \cdots$$

By truncating the previous relation to the mth power of $|\Omega|^{1/3}$, one can consider the approximate inversion[2]

$$u_i \cong A^{(m)} \bar{u}_i = \overline{A^{(m)} u_i} \tag{7}$$

and define the deconvolved filtered variable as

$$\tilde{u}_i = \overline{A^{(m)} u_i} \tag{8}$$

[2] For the sake of simplicity, when it is possible, the explicit dependence on $\boldsymbol{x}$ is omitted.

It is worth noting that Equation (7) is still based on a commutative property, which holds for constant coefficients (5).

By applying the above deconvolution procedure onto the integral balance equation (3), one has

$$\frac{\partial \tilde{u}_i}{\partial t} = \frac{1}{|\Omega|} \int_{\partial\Omega} \mathrm{d}S \, n_k A^{(m)} f_{ik} \tag{9}$$

or, equivalently, the corresponding local form (4) as

$$\frac{\partial \tilde{u}_i}{\partial t} = \frac{\partial \tilde{f}_{ik}}{\partial x_k} \tag{10}$$

The problem is well posed by considering proper boundary conditions for $\tilde{u}_i$. These latter are provided by evaluating (8) on $\partial\Omega$, according to the de-averaging order m. Following a classical approach [19], Equation (10) can be integrated via a fractional time step method: first, an intermediate non-solenoidal velocity field is obtained by neglecting the pressure term; then, the solution of an elliptic equation, for a modified pressure variable, provides the irrotational velocity correction that imposes the divergence-free velocity constraint $\partial \tilde{u}_i / \partial x_i = 0$, as was shown in De Stefano *et al.* [7]. No explicit boundary conditions for the pressure variable are necessary, the knowledge of $\tilde{u}_i$ on $\partial\Omega$ being sufficient [19].

Motivations leading to modify the balanced variable must be found in a couple of fundamental issues. The first one is that Equation (10) can be adopted to develop high-order schemes for DNS calculations, by exploiting the higher accuracy of the modified velocity variable [6–8]. The second one is that the same equation can be adopted for LES calculations, where the solution components at high resolved wavenumbers are less affected by the smoothness of the filter, as will be clearly highlighted in the next section.

Moreover, the de-filtering procedure is adopted in order to represent the balance of a new filtered variable in such a way that CV formulation can produce more accurate numerical results. In this context, by looking at (10) as an LES equation, one can consider $\tilde{u}_i$ as the solution of the explicitly pre-filtered Navier–Stokes equations wherein the filtered variable is defined by means of the following spatial convolution [10]

$$\tilde{u}_i(\boldsymbol{x}) = \int \mathrm{d}\boldsymbol{x}' \, G^{(m)}(\boldsymbol{x} - \boldsymbol{x}';\ \Delta) u_i(\boldsymbol{x}') \tag{11}$$

with a filter function $G^{(m)}$ related to the application of both the mth order reconstruction and the cell-averaging. By expliciting the resolved terms, Equation (10) is re-written as

$$\frac{\partial \tilde{u}_i}{\partial t} = \frac{\partial}{\partial x_k} \left(-\tilde{u}_i \tilde{u}_k - \tilde{\tau}_{ik} - \delta_{ik} \frac{\tilde{p}}{\rho_0} + \nu \frac{\partial \tilde{u}_i}{\partial x_k} \right) \tag{12}$$

which represents the conservative local form of the LES equations to be solved. However, in our approach, we consider the corresponding 'weak' form of (12) provided by a CV integration. In the previous equation, the SGS stresses

$$\tilde{\tau}_{ik} = \widetilde{u_i u_k} - \tilde{u}_i \tilde{u}_k \tag{13}$$

have been defined as presented in Vasilyev *et al.* [9]. Finally, in the LES approach, one has to introduce a modeling procedure to express (13) in terms of the resolved field.

The above approach differs from the others appearing in the recent literature, wherein the approximate evaluation of the SGS stress in the top-hat filtered momentum equation is obtained via a deconvolution, e.g. [14]. In the letter [13], such a procedure is recognized as leading to an evolution equation that is simply related to Equation (12) by setting $\tilde{\tau}_{ik} = 0$, i.e. without considering the SGS stresses for the new filtered variable. This turns out to be equivalent to solve the top-hat filtered ($m = 0$) LES equations with a generalized scale-similarity model.

Furthermore, it is worth noticing how the approximate inversion can be seen in the framework of high-order reconstruction techniques, such as, for example, the essentially non-oscillatory (ENO) reconstruction [20]. Actually, differently from our procedure, in the ENO approach the volume averaged variable is not modified, namely the de-averaging order remains $m = 0$. In fact, ENO reconstruction acts on the right-hand side (RHS) of Equation (4) in order to provide a better approximation for the flux function. More details about high-order reconstruction techniques can be found, for example, in Grasso and Meola [21].

3. A THEORETICAL ANALYSIS FOR THE ONE-DIMENSIONAL CASE

In this section, we develop a theoretical study of the described approach in one spatial dimension; then, we apply it to the Burgers' equation in order to highlight the effects of the present filtering procedure.

3.1. A high-order filtering procedure

The analytical form of the inverse operator $A^{(m)}$ in Equation (7) and that one of the filter function in (11) are herein derived. The result of the de-averaging operation will be a better representation of the resolved field at high wavenumbers. Thus, the local-average based reconstruction procedure can be seen as a high-order modification of the top-hat filtering. Let us consider the reconstruction operator (6) truncated up to an even order $m = 2n$, with $\Omega(x) = [x - \Delta/2, x + \Delta/2]$. By applying it to the velocity field u, one obtains the following differential expression

$$R_x^{(m)} u = -\frac{1}{\Delta} \sum_{l=1}^{m} \frac{1}{l!} u^{(l)}(x) \int_{x-\Delta/2}^{x+\Delta/2} \mathrm{d}\xi \, (\xi - x)^l = -\sum_{p=1}^{n} \frac{(\Delta/2)^{2p}}{(2p+1)!} u^{(2p)}(x)$$

In order to find the expression for the inverse operator $A^{(m)}$, the problem will be stated as follows: find the solution $\tilde{u}$ of the differential equation

$$[I_x - R_x^{(m)}]\tilde{u} = \bar{u}(x) \tag{14}$$

with $\bar{u}$ representing a known source term. In Appendix A, by solving Equation (14), the inverse operator is shown to be

$$A_x^{(m)} = I_x + C_2 \frac{\mathrm{d}^2}{\mathrm{d}x^2} + C_4 \frac{\mathrm{d}^4}{\mathrm{d}x^4} + \cdots \tag{15}$$

with $C_2 = -\Delta^2/24$ and $C_4 = 7\Delta^4/5760$. According to Equations (7) and (15), the actual filtered velocity can be written as

$$\tilde{u}(x) = \frac{1}{\Delta} \int_{x-\Delta/2}^{x+\Delta/2} \mathrm{d}\xi \sum_{p=0}^{n} C_{2p} u^{(2p)}(\xi) = \sum_{p=0}^{n} C_{2p} \bar{u}^{(2p)}(x)$$

having assumed $C_0 = 1$.

The main features of the present filtering procedure can be better discussed in Fourier space, where the above convolution is simply transformed in

$$\hat{\tilde{u}}(\kappa) = \hat{G}^{(m)}(\kappa; \Delta)\hat{u}(\kappa) = \left[\sum_{p=0}^{n} (-1)^p C_{2p} \kappa^{2p} \right] \hat{G}^{(0)}(\kappa; \Delta)\hat{u}(\kappa)$$

where the transformed top-hat filter $\hat{G}^{(0)}(\kappa) = \sin(\kappa\Delta/2)/(\kappa\Delta/2)$ has been defined. From this equation we can recognize the mth order transformed filter function according to

$$\hat{G}^{(m)}(\kappa; \Delta) = \left[\sum_{p=0}^{n} (-1)^p C_{2p} \kappa^{2p} \right] \hat{G}^{(0)}(\kappa; \Delta) \tag{16}$$

In Figure 1 the filter functions $\hat{G}^{(2)}$ and $\hat{G}^{(4)}$ are reported, together with the transformed top-hat function $\hat{G}^{(0)}$. It clearly appears that for $\kappa\Delta < 2\pi$, the high wavenumber components are as better represented as higher is the de-averaging order m. The reconstruction can be interpreted as a de-filtering operation in the sense that one can recover information otherwise lost by averaging the velocity field. This way, by making the filter as close as possible to the spectral cut-off, the large scales are less affected by filtering procedure and the SGS stress becomes less important at resolved wavenumbers.

As a matter of fact, Equation (16) does no longer provide a filter function as generally thought, unless it is adopted in conjunction with a spectral cut-off, as will be addressed in the following in terms of an error analysis.

3.2. The high-order filtered Burgers' equation

In this section, the Burgers' equation will be considered as a model equation in order to examine in details the present approach. In fact, owing to its non-linear character, the essential features of the actual filtering procedure can be usefully investigated [22]. At present, an analysis limited to the evaluation of the spatial accuracy is carried out. Let us consider the equation

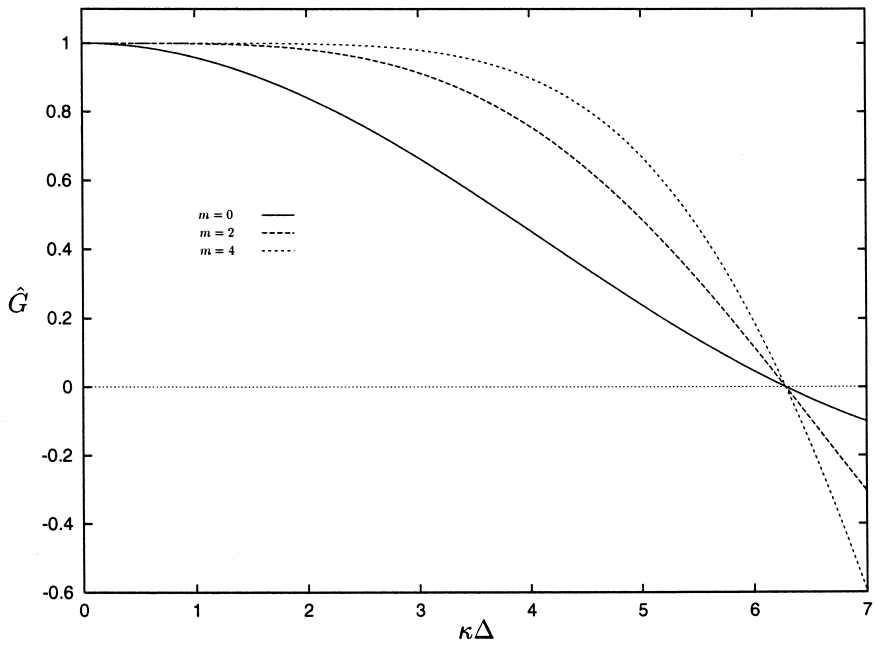

Figure 1. Modified filter functions in wavenumbers space, for various de-averaging orders.

$$\frac{\partial u}{\partial t} = \frac{\partial f(u)}{\partial x}$$

with $f = -u^2/2$ and filter it according to definition (7)

$$\frac{\partial \tilde{u}}{\partial t} = \frac{1}{\Delta}\left[A^{(m)}\left(-\frac{\tilde{u}^2}{2} - \frac{\tau}{2} \right) \right]_{x-\Delta/2}^{x+\Delta/2} \tag{17}$$

having defined, according to (13), the SGS stress

$$\tau = u^2 - \tilde{u}^2 \tag{18}$$

The effects of such a procedure are investigated by applying it on a periodic function $u(x)$ in a domain of length L. Let us consider the velocity field expressed in terms of its Fourier components

$$u(x) = \sum_k \hat{u}_k e^{i\kappa x} \tag{19}$$

where $\kappa = k2\pi/L$ and the coefficients $\hat{u}_k$ are assumed to be $\sqrt{E(\kappa)/2}\,\mathrm{e}^{\mathrm{i}\theta_k}$ with θ_k random phases, uniformly distributed in $[-\pi, \pi)$. As model energy spectrum, one can consider the following [12]:

$$E(\kappa) = a\kappa^{-5/3} M(\kappa^4/\kappa_1^4) M(\kappa^{5/3}\,\mathrm{e}^{-\kappa/\kappa_2}) \tag{20}$$

where $M(\xi) = 1 - \mathrm{e}^{-\xi}$ and the constant a is chosen in order to ensure $\int_0^{+\infty} \mathrm{d}\kappa\, E(\kappa) = 1$. In particular, this spectrum shows an inertial subrange with the same slope of a typical turbulent flow.

Given a filter width Δ, the filtered velocity is computed according to

$$\tilde{u}(x) = \sum_k \hat{G}^{(m)}(\kappa; \Delta)\hat{u}_k\,\mathrm{e}^{\mathrm{i}\kappa x}$$

with $\hat{G}^{(m)}$ from Equation (16). In order to address the effects of the actual filtering procedure in physical space, let us assume $L = 2\pi$ and Equation (19) extended up to $k_{\max} = 1024$ and consider, for various de-averaging orders m, the ratio

$$\epsilon_1 = \frac{\|\partial_x f - \partial_x \tilde{f}\|}{\|\partial_x f\|}$$

where, from now on, $\|\cdot\|$ stands for the L_2-norm. In Figure 2, this ratio is reported versus the filter width Δ, having fixed $\kappa_1 = 10$ and $\kappa_2 = 40$ in Equation (20). The figure shows convergence rates according to the foreseen order. It is worth noting that the de-filtering operation allows us to recover a higher accuracy of the filtered variable while, by adopting a classical top-hat formulation, one would otherwise keep it to the second-order. From the analysis of the figure, one can also observe a characteristic trend: the curves intersect so that, for large values of Δ, the ratio ϵ_1 corresponding to $m > 0$ becomes greater than that one corresponding to $m = 0$. In fact, when $\kappa\Delta > 2\pi$, the modified filter functions apply also on wavenumbers for which the difference $1 - \hat{G}$ increases for increasing m (see Figure 1). For a function u having a given spectrum extending up to $k_{\max}$, we can regard the intersecting value $\bar{\Delta}$ as the one providing the largest filter width we can adopt, if we want to keep the better accuracy of our procedure. As expected, it results in $\bar{\Delta} > \pi/k_{\max}$, caused by the doubling on the wavenumbers range, owing to the non-linearity. We will show in the following that such issues are modified by introducing a discrete representation of the flux function. By computing the previous ratio with respect to the resolved field $\tilde{u}$, i.e. by neglecting the SGS term in Equation (17), one can examine the behavior of our procedure within the framework of a DNS.

$$\epsilon_2 = \frac{\|\partial_x f - \partial_x(-\tilde{u}^2/2)\|}{\|\partial_x f\|}$$

From Figure 3 it results evident that, to practically carry out a DNS, it is reasonable to resort to a higher order reconstruction together with a grid size that, in principle, guarantees that $k_{\max}\Delta < \pi$. It also appears that, for very large Δ, top-hat filtering keeps the magnitude of the

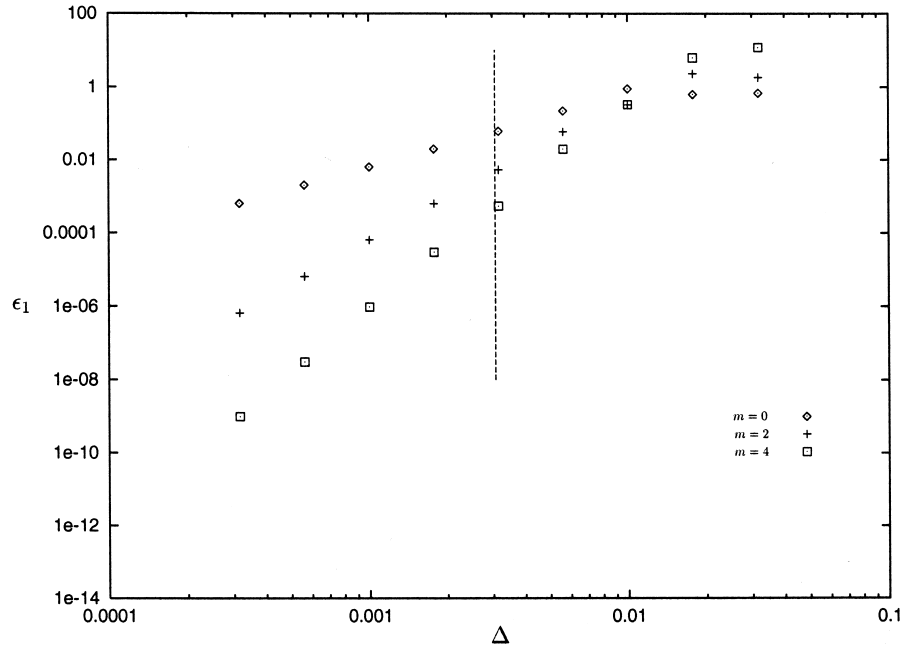

Figure 2. Filtering effects, ϵ_1 versus Δ for various de-averaging orders; the vertical line corresponds to $\Delta = \pi/\kappa_{\max}$.

errors at order one, while amplifications of the errors are produced by the modified filtering procedure.

3.3. SGS stress analysis

In this section, let us examine the absolute importance of the SGS stress to be modeled in Equation (17). The issue is still better discussed in Fourier space: the SGS stress (18), corresponding to an order m_1, can be written as

$$\tau(x) = \sum_k \mathrm{e}^{\mathrm{i}\kappa x} \sum_{l+n=k} \Theta_{l,n}^{(m_1)} \hat{u}_l \hat{u}_n$$

where

$$\Theta_{l,n}^{(m_1)} = 1 - \hat{G}^{(m_1)}(l)\hat{G}^{(m_1)}(n)$$

By exploiting the fact that random phases are uniformly distributed, one has the corresponding spectrum for τ [12]

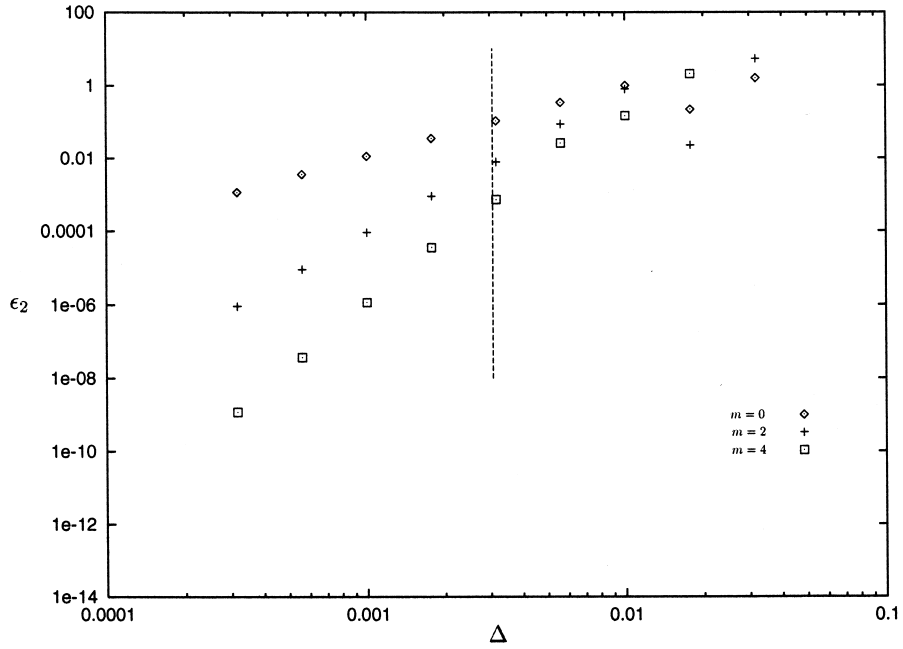

Figure 3. Filtering effects, ϵ_2 versus Δ for various de-averaging orders; the vertical line corresponds to $\Delta = \pi/\kappa_{\max}$.

$$\mathscr{E}_\tau(\kappa) = \sum_{l+n=k} [\Theta_{l,n}^{(m_1)}]^2 E(l)E(n) \tag{21}$$

For a filter width $\Delta = 0.02$, the above spectra are reported in Figure 4, for various filtering orders m_1. As clearly appears, for increasing orders, the stress term to be modeled becomes less important in the resolved range. In particular, for the largest resolved scales, it becomes also one decade lower with respect to the classical top-hat formulation. Finally, it becomes as closer to the spectral cut-off as higher is the de-filtering order.

The approximate inversion of the averaging operator introduced in the previous section can be used to develop a high-order SGS model for the LES equation (17). According to the similarity model of Bardina [23], the SGS stress can be approximated by substituting the resolved field instead of the original one into the definition (18)

$$\tau^{(\mathrm{mod})} = \tilde{u}^2 - \tilde{\tilde{u}}^2 \tag{22}$$

Thus, the modeled SGS stress can be expressed as

$$\tau^{(\mathrm{mod})}(x) = \sum_k \mathrm{e}^{\mathrm{i}\kappa x} \sum_{l+n=k} \Theta_{l,n}^{(m_1,m_2)} \hat{u}_l \hat{u}_n$$

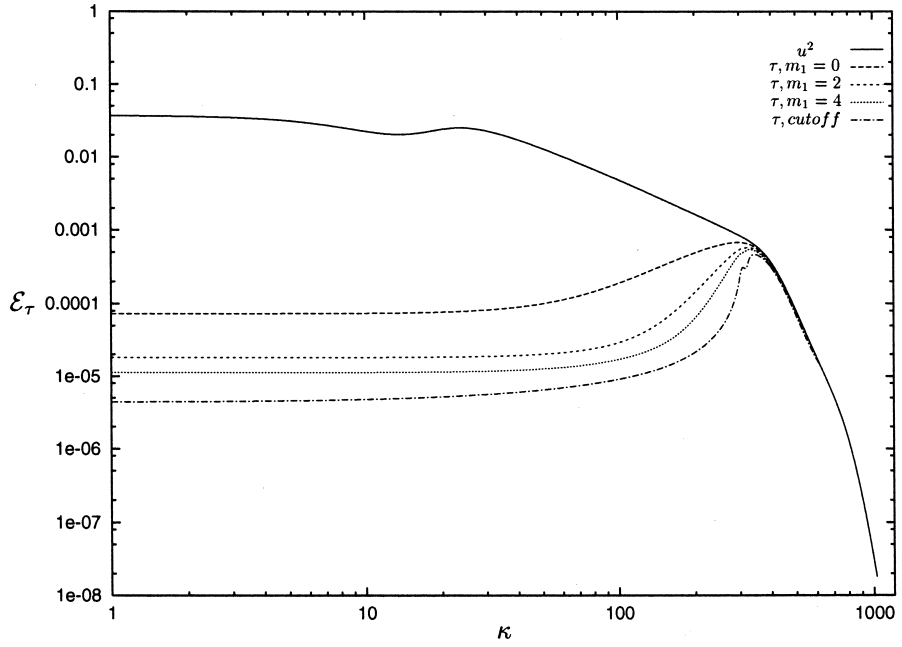

Figure 4. Spectrum of the exact SGS stresses, for various de-averaging orders; the stress corresponding to the spectral cut-off and the exact spectrum of u^2 are also reported.

with

$$\Theta_{l,n}^{(m_1,m_2)} = \hat{G}^{(m_2)}(l)\hat{G}^{(m_2)}(n)\Theta_{l,n}^{(m_1)}$$

In order to examine the approximation of the model, one can compare the following spectrum

$$\mathscr{E}_{\tau\,(\mathrm{mod})}(\kappa) = \sum_{l+n=k} [\Theta_{l,n}^{(m_1,m_2)}]^2 E(l)E(n)$$

with respect to the exact one (21). As a matter of fact, for $m_2 = m_1$, the modeled stress (22) tends to zero for increasing filtering orders, since it exactly vanishes for the idempotent sharp cut-off filter; therefore, the dissipative part of the mixed model becomes more important.

Recently, the adoption of an analogous inversion has been proposed in [11–14] in order to define a generalized similarity model, by substituting, into the definition of the SGS stress for the top-hat filter, the unfiltered velocity u with the de-filtered velocity $\tilde{u}$ namely, by considering $\tau^{(\mathrm{mod})} = \tilde{u}^2 - \tilde{\tilde{u}}^2$. Actually, this corresponds to fix $m_1 = 0$ and $m_2 > 0$ in the previous equations. As a matter of fact, even when $m_1 > 0$, one can adopt a suitable inversion of the resolved field, with $m_2 \geq m_1$, in order to better approximate the SGS stress.

In Figure 5, we report the ratio $\mathscr{E}_{\tau(\mathrm{mod})}/\mathscr{E}_{\tau}$ for a generalized similarity model with $m_1 = 0$ and $m_2 = 4$ and for the similarity model (18), for various orders $m_1 = m_2$. As expected, in the first case, a better approximation of the corresponding exact SGS stress is obtained. However, as already illustrated in Figure 4, the absolute importance of the stress to be modeled decreases for increasing m_1.

Finally, it is worth remarking that the above analytical tests must be considered only as indicative of the capability of the actual model to be used in LES of turbulent flows. In particular, the numerical discretization could produce strong modifications to the present analysis.

4. NUMERICAL SCHEME ANALYSIS

In this section, we analyze the numerical implementation of the present filtering procedure. It is worth stressing that the discrete representation of the balanced variable introduces a grid cut-off on the actual resolved spectrum, with a cut-off wavenumber depending on the mesh size. Given a set of pointwise values, in the corresponding nodal points of some discretization of the one-dimensional domain, several local Lagrangian polynomial approximations are

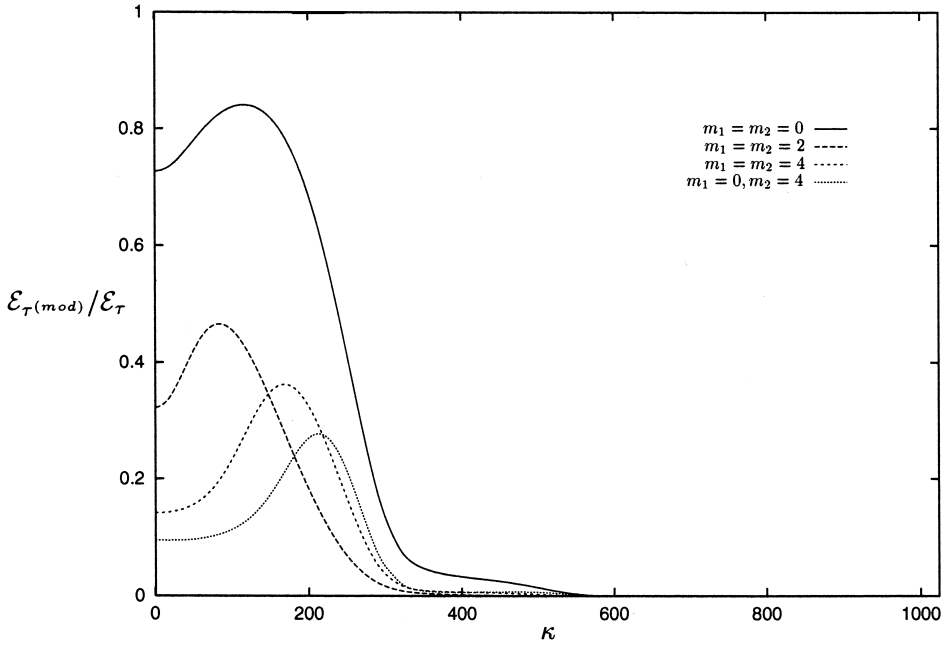

Figure 5. Ratio between modeled and exact SGS stress spectra, for various de-averaging orders. The ratio for the generalized similarity model is also reported.

adopted for the unknown variable, on symmetric or non-symmetric supports. This way, one can evaluate the effects of a spatial discretization of Equation (17) with respect to the previous analytical results. In the next sections, we analyze the application of various schemes for the velocity field provided by Equation (19), by disregarding the SGS term in Equation (17).

4.1. The linear transport equation

For the sake of clarity, we first briefly consider the linear wave equation (having assumed unitary transport velocity), for which the numerical derivative of the flux is written, for the general nodal position $x_j = jh$

$$\left(\frac{\partial \tilde{u}}{\partial t}\right)_j = \left(\frac{\partial \tilde{f}}{\partial x}\right)_j \equiv \frac{1}{h}\,[A^{(m)}(-u)]_{j-1/2}^{j+1/2}$$

By considering on each one of the CV sections a polynomial of degree g for the interpolation of the balanced variable: $u \cong \Sigma_{k=0}^{g} p_k x^k$, it is shown that some well-known FD formula may be reviewed within the framework of the present formulation. Let us first consider the class of central schemes, obtained by an interpolation on symmetric supports. By considering $g = 1$, one obtains the well-known second-order central difference formula

$$\left(\frac{\delta \tilde{f}}{\delta x}\right)_j = -\frac{u_{j+1} - u_{j-1}}{2h} \tag{23}$$

that corresponds to the implicit top-hat filtering of width $2h$ [24]. If one wants to apply the reconstruction operation, for example for $m = 2$, it is necessary to consider at least $g = 3$; thus, one obtains

$$\left(\frac{\delta \tilde{f}}{\delta x}\right)_j = -\frac{-u_{j+2} + 8u_{j+1} - 8u_{j-1} + u_{j-2}}{12h} \tag{24}$$

that is a well-known fourth-order FD expression for the first derivative [25]. One can conclude that, analogously to Equation (23), Equation (24) can be interpreted as a numerical approximation to the high-order filter introduced in the previous sections. Moreover, for increasing polynomial degrees, together with a proper reconstruction, one obtains higher order central FDs.

As concerns the upwind schemes, if we consider on the CV sections a second-degree polynomial and assume positive velocity, by applying the de-averaging operation with $m = 2$, one obtains a classical third-order upwind FD approximation for the first derivative [26,27]

$$\left(\frac{\delta \tilde{f}}{\delta x}\right)_j = -\frac{2u_{j+1} + 3u_j - 6u_{j-1} + u_{j-2}}{6h} \tag{25}$$

Fifth-order FD schemes can be obtained by considering $g = m = 4$; in this case, one can choose two different non-symmetric interpolation supports. In the first case, one obtains

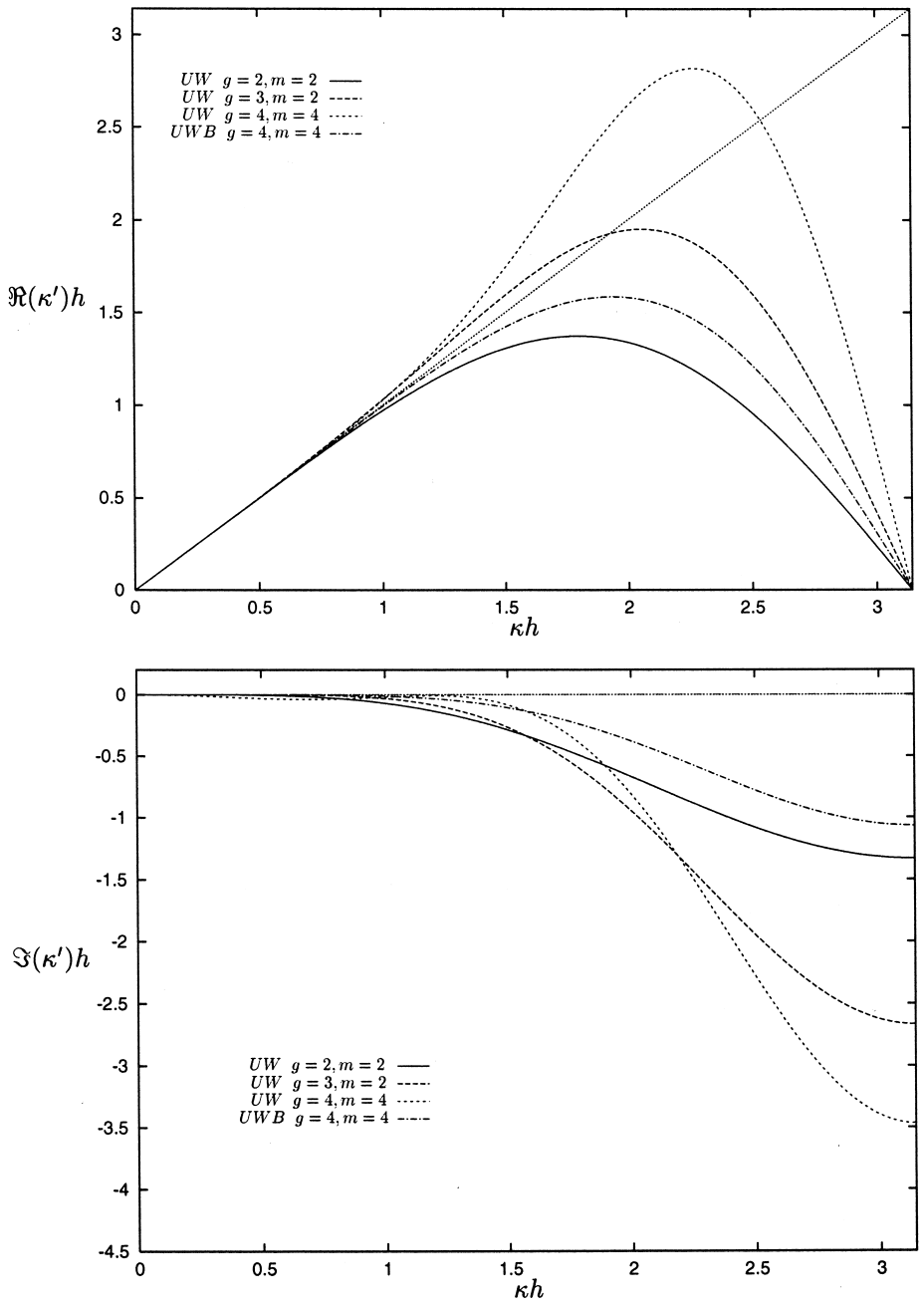

Figure 6. Modified wavenumbers for upwind schemes of third-, fourth- and fifth-order: real part and coefficient of the imaginary part.

$$\left(\frac{\delta\tilde{f}}{\delta x}\right)_j = -\frac{12u_{j+1} + 65u_j - 120u_{j-1} + 60u_{j-2} - 20u_{j-3} + 3u_{j-4}}{60h}$$

while in the second one, referred to as an upwind-biased scheme [26], one has

$$\left(\frac{\delta\tilde{f}}{\delta x}\right)_j = -\frac{-3u_{j+2} + 30u_{j+1} + 20u_j - 60u_{j-1} + 15u_{j-2} - 2u_{j-3}}{60h}$$

As is well known, upwind numerical derivatives show a modified wavenumber having a non-vanishing imaginary part (see Appendix B), which is more important at high wavenumbers. This fact reflects a truncation error of dissipative nature. In Figure 6 the corresponding modified wavenumbers are reported in terms of both real and imaginary parts. The upwind-biased scheme, owing to its more symmetric support, shows the smallest error along the imaginary axis, while maintaining a good approximation on the real axis.

4.2. The non-linear transport equation

In the non-linear case, the equation to discretize is

$$\left(\frac{\partial\tilde{u}}{\partial t}\right)_j = \left(\frac{\partial\tilde{f}}{\partial x}\right)_j \equiv \frac{1}{h}\left[A^{(m)}\left(-\frac{u^2}{2}\right)\right]_{j-1/2}^{j+1/2} \tag{26}$$

At this point, the variable to interpolate between the advective flux and the velocity must be chosen. As a matter of fact, the latter being the balanced variable, the second choice appears more consistent. This way, by choosing the polynomial interpolation already adopted in the linear case, and a suitable de-averaging order, one obtains various numerical schemes. For example, in the case of symmetric supports, for $g = 1$ and $m = 2$, one has

$$\left(\frac{\delta\tilde{f}}{\delta x}\right)_j = \frac{1}{h}\sum_{p=-1}^{1}\sum_{q=p}^{1} c_{pq}u_{j+p}u_{j+q} \tag{27}$$

with the coefficients c_{pq} summarized in Table I. For $g = 3$, $m = 4$, the sum ranges from -2 up to 2 and the corresponding coefficients are reported in Table II. It is particularly interesting to evaluate the modified equation, i.e. the actual partial differential equation solved by the numerical scheme

$$\frac{\partial u}{\partial t} = \frac{\partial}{\partial x}\left(-\frac{u^2}{2}\right) + L(x, t)$$

where L is the local truncation error. For the previous two schemes, it results respectively

$$L(x, t) = -\frac{h^2}{6}\frac{\partial}{\partial x}\left(u\frac{\partial^2 u}{\partial x^2}\right) + O(h^4)$$

Table I. Coefficients c_{pq} for the second-order central scheme

c_{pq}	$q=-1$	0	$+1$
$p=-1$	$\frac{1}{12}$	$\frac{1}{3}$	0
0		0	$-\frac{1}{3}$
$+1$			$-\frac{1}{12}$

Table II. Coefficients c_{pq} for the fourth-order central scheme

c_{pq}	$q=-2$	-1	0	$+1$	$+2$
$p=-2$	$\frac{269}{69120}$	$-\frac{461}{11520}$	$-\frac{691}{11520}$	$\frac{307}{34560}$	0
-1		$\frac{169}{1728}$	$\frac{599}{1152}$	0	$-\frac{307}{34560}$
0			0	$-\frac{599}{1152}$	$\frac{691}{11520}$
$+1$				$-\frac{169}{1728}$	$\frac{461}{11520}$
$+2$					$-\frac{269}{69120}$

$$L(x,t)=\frac{h^4}{30}\frac{\partial}{\partial x}\left(u\frac{\partial^4 u}{\partial x^4}\right)+O(h^6)$$

Now, consider the upwind schemes based on second- and fourth-degree polynomials, associated with a de-filtering operation of consistent order ($m=g$). Equation (27) involves, for $g=m=2$, the nodes $(j-2,\ldots,j+1)$ and the corresponding coefficients are reported in Table III. For $g=m=4$, the nodes $(j-4,\ldots,j+1)$ and $(j-3,\ldots,j+2)$ are involved for upwind and upwind-biased schemes respectively. According to such numerical schemes, the corresponding truncation errors are

$$L(x,t)=-\frac{h^3}{12}\frac{\partial}{\partial x}\left(u\frac{\partial^3 u}{\partial x^3}\right)+O(h^4)$$

$$L(x,t)=-\frac{h^5}{30}\frac{\partial}{\partial x}\left(u\frac{\partial^5 u}{\partial x^5}\right)+O(h^6)$$

Table III. Coefficients c_{pq} for the third-order upwind scheme

c_{pq}	$q=-2$	-1	0	$+1$
$p=-2$	$\frac{5}{384}$	$-\frac{13}{96}$	$-\frac{11}{192}$	0
-1		$\frac{37}{128}$	$\frac{1}{2}$	$\frac{11}{192}$
0			$-\frac{37}{128}$	$-\frac{35}{96}$
$+1$				$-\frac{5}{384}$

$$L(x,t) = \frac{h^5}{60}\frac{\partial}{\partial x}\left(u\frac{\partial^5 u}{\partial x^5}\right) + O(h^6)$$

It is worth remarking that all the above truncation errors show a leading term in conservative form, as is expected having de-filtered in a consistent manner. On the contrary, we verified that, by choosing an interpolation degree non-consistent with the reconstruction order, a non-conservative leading term is obtained. However, as has been noted in Morinishi *et al.* [28], the conservative form of the momentum balance equation does not guarantee *a priori* energy conservation, unless the continuity constraint is numerically preserved.

A comparison of the performances of the various schemes, for some grid spacing value h, is reported in Figure 7, in terms of the ratio

$$\epsilon \equiv \frac{\|\partial_x f - \delta_x \tilde{f}\|}{\|\partial_x f\|}$$

Clearly, the slopes of the error curves are no longer those corresponding to the analytical tests in Figure 2. However, one can conclude that higher order conservative schemes can be

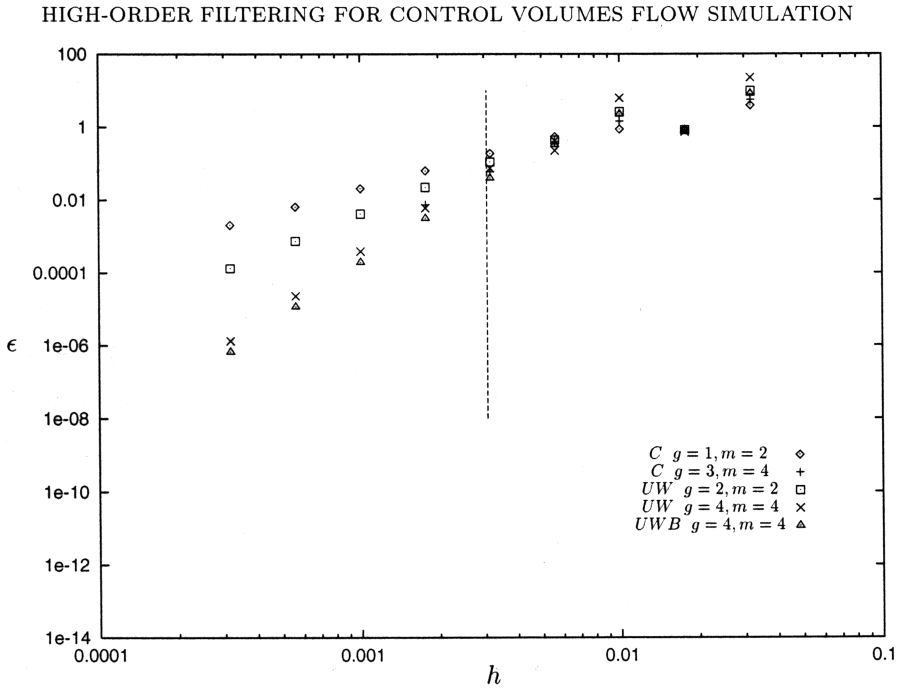

Figure 7. Discretization errors versus the grid spacing h for some central (C), upwind (UW) and upwind-biased (UWB) schemes. The vertical line corresponds to $h = \pi/\kappa_{\max}$.

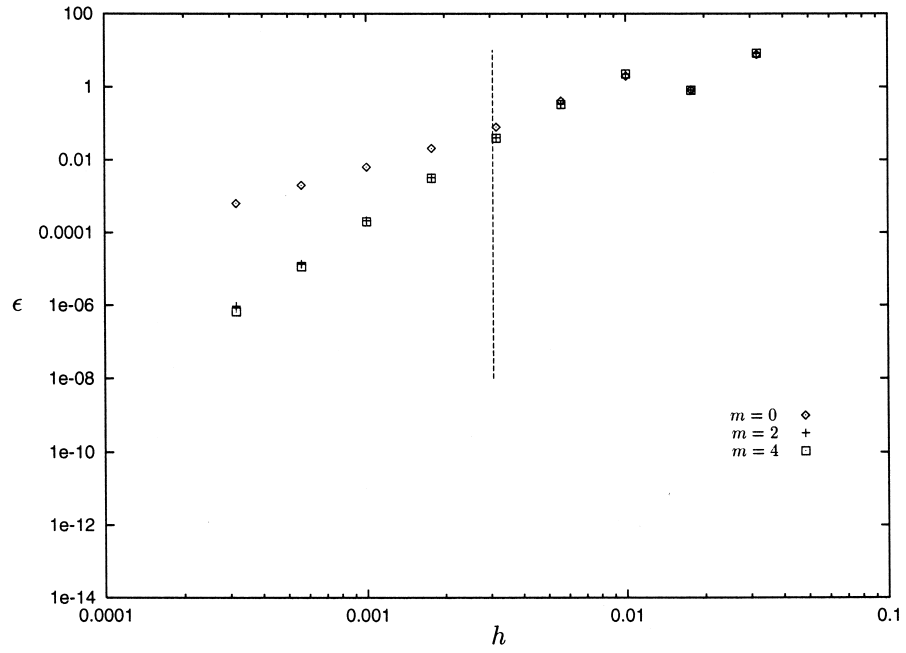

Figure 8. Discretization errors for the fourth-order upwind-biased scheme, for various de-averaging orders. The vertical line corresponds to $h = \pi/\kappa_{\max}$.

successfully obtained by means of the application of the de-averaging operator $A^{(m)}$. It is interesting to separately evaluate the effects of both de-filtering and interpolation orders. The first effect is analyzed in Figure 8 for a fourth-degree polynomial on a upwind-biased stencil and various orders m. In particular, the change of slope appears quite important between $m = 0$ and 2, well representing the filter change from $\bar{u}$ to $\tilde{u}$. A further improvement for $m = 4$ appears only for smaller filter widths. Finally, in Figure 9 are reported the curves obtained for upwind schemes for various polynomial degrees without reconstruction. The slope remains the same for all curves, remaining the filtered variable $\bar{u}$, whatever the interpolation order. This feature demonstrates what we addressed the ENO reconstruction: without deconvolving all terms of the momentum equation, higher order flux reconstruction alone can not change the volume average ($m = 0$) accuracy of the top-hat filter.

4.3. Spectral distribution of numerical errors

In the simulation of turbulent flows the accuracy study must be completed by spectral analysis. In fact, the accuracy of the scheme generally decreases for increasing wavenumbers. Given the velocity field in terms of its discrete Fourier components, for a grid size $h = 2\pi/N$

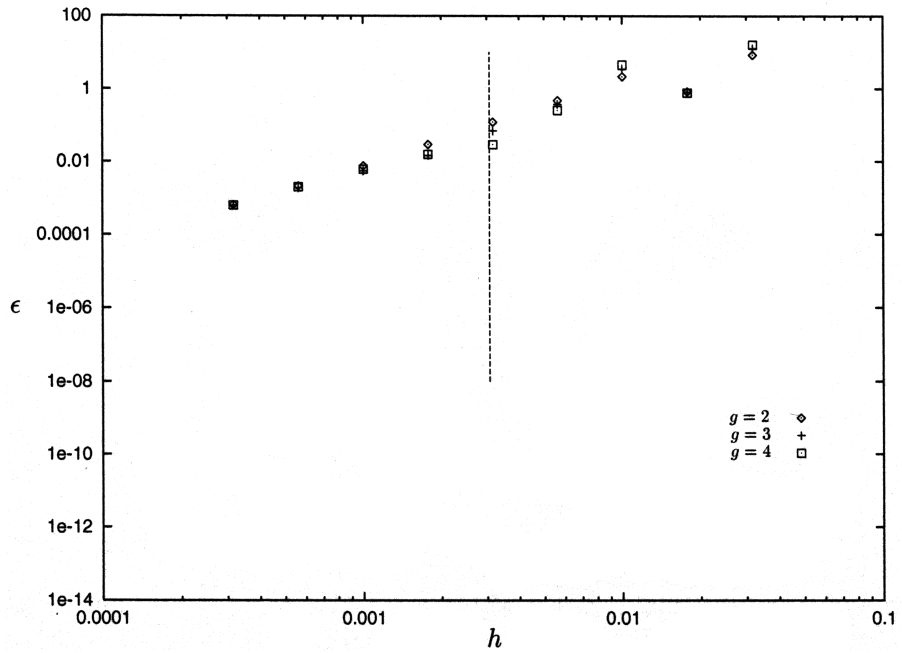

Figure 9. Discretization errors for upwind schemes in the absence of de-averaging, for various interpolation orders. The vertical line corresponds to $h = \pi/\kappa_{\max}$.

$$u_j = \sum_k \hat{u}_k \, \mathrm{e}^{\mathrm{i}(2\pi/N)kj}$$

With $k = -N/2, \ldots, N/2$, the exact flux derivative in (26) is simply expressed by

$$\left(\frac{\partial f}{\partial x}\right)_j = i \sum_k d_k \, \mathrm{e}^{\mathrm{i}(2\pi/N)kj}$$

the real coefficients d_k being defined as

$$d_k \equiv -\frac{k}{2} \sum_{l+n=k} \hat{u}_l \hat{u}_n.$$

It is worth highlighting that the previous expression has been obtained by removing the aliasing errors; in other words, we considered the k-th Fourier coefficient of u^2: $\Sigma_{l+n=k} \, \hat{u}_l \hat{u}_n + \Sigma_{l+n=k\pm N} \, \hat{u}_l \hat{u}_n$, by neglecting the second sum in this expression.

On the other hand, the application of a numerical scheme provides

$$\left(\frac{\delta \tilde{f}}{\delta x}\right)_j \equiv \mathrm{i} \sum_k d'_k \, \mathrm{e}^{\mathrm{i}(2\pi/N)kj} \tag{28}$$

where the modified coefficients d'_k depend on the actual adopted scheme.[3] Since each numerical formula for the evaluation of the flux derivative is expressed as in (27), it can be analyzed in Fourier space by considering the modified coefficients

$$d'_k = -\frac{\mathrm{i}}{h} \sum_{l+n=k} \hat{u}_l \hat{u}_n \sum_p \sum_{q \geq p} c_{pq}\, \mathrm{e}^{\mathrm{i}(2\pi/N)(lp+nq)}$$

that are not real for upwind schemes.

Therefore, the effects of different numerical discretizations can be evaluated by examining the difference between the complex coefficients d'_k and d_k. For central schemes this difference involves only the real part; it is reported for the second- and fourth-order scheme in Figure 10, by fixing $N = 1024$ grid points. The effect of filter change in terms of the numerical error is quite clear. For upwind schemes a numerical error on the imaginary axis also appears, as

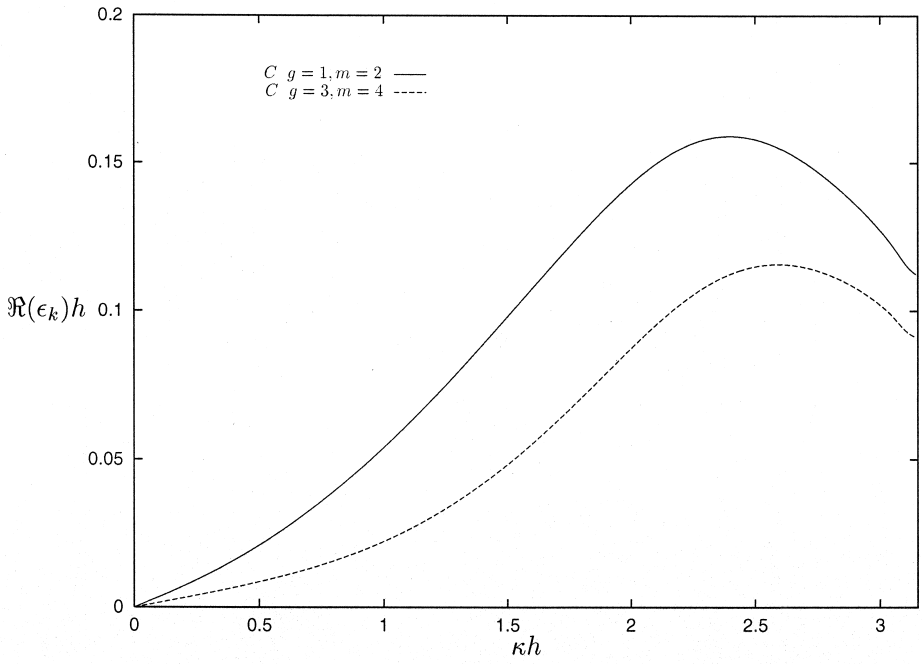

Figure 10. Discretization errors ϵ_k versus grid spacing h, for the second- and fourth-order central schemes. In this case, only the real part is involved.

[3] As a matter of fact, in this form, the modified coefficients depend also on the velocity spectrum, even if one could change the definition (28) to by-pass this problem.

reported in Figure 11. In this figure, as well as in the next ones, each point along a curve represents the error, in the complex plane, for a given value of κ, starting with $\kappa = 0$ at the origin. From the examination of Figure 11, the fifth-order upwind-biased scheme clearly appears as the most accurate. Finally, Figures 12 and 13 show the effects, in wavenumbers space, of de-filtering and interpolation orders. In particular, the error on the imaginary axis introduced by upwind schemes, gets worse either by increasing m, for a given interpolation order (see Figure 12) or by increasing g, in the absence of reconstruction (see Figure 13). On the other hand, increasing m or g, provides a better trend of the error on the real axis.

One of the most important features of the actual schemes is that they are conservative. It is interesting to make a comparison with high-order schemes in non-conservative form. Let us consider those obtained from the fourth-order central scheme and the fifth-order upwind-biased scheme adopted in the linear case (see also [26])

$$\left(-u\frac{\delta u}{\delta x}\right)_j = -\frac{u_j(-u_{j+2}+8u_{j+1}-8u_{j-1}+u_{j-2})}{12h}$$

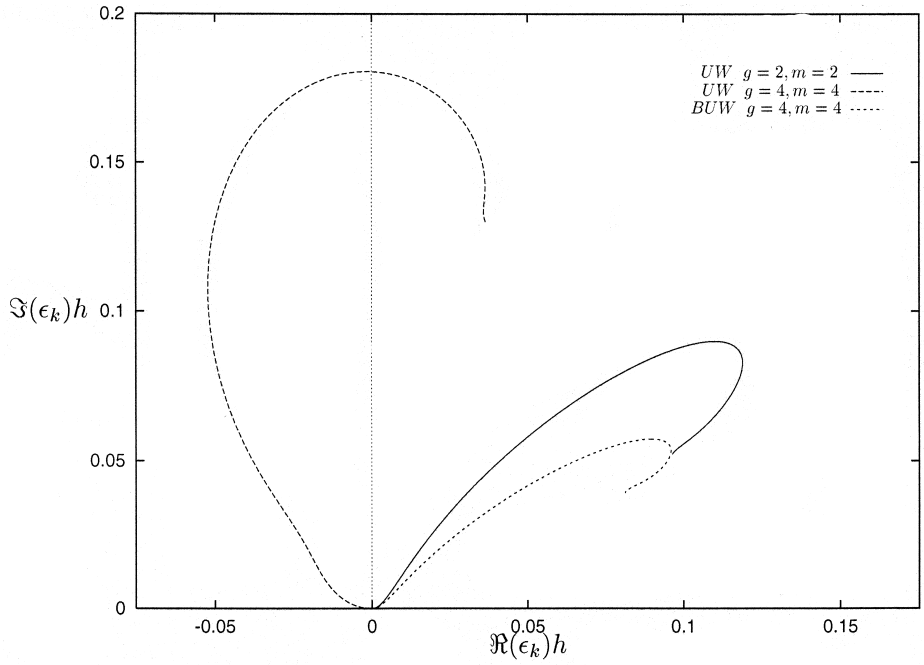

Figure 11. Discretization errors ϵ_k for the third- and fifth-order upwind (UW) schemes and the fifth-order upwind-biased (UWB) scheme. Each point along the curves corresponds to a given value of κ.

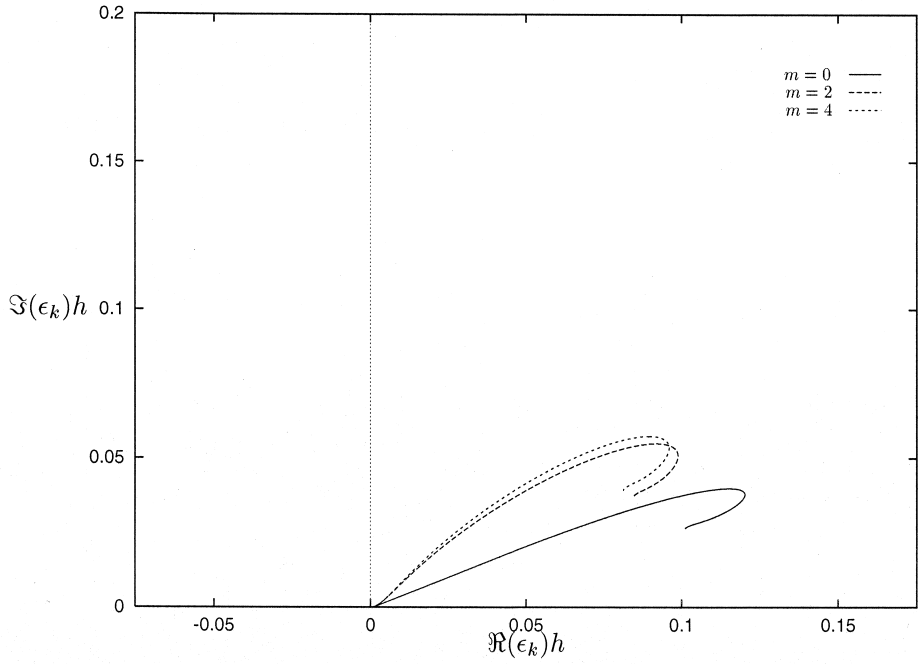

Figure 12. Discretization errors ϵ_k for the upwind-biased scheme, for $g = 4$ and various de-averaging orders. Each point along the curves corresponds to a given value of κ.

$$\left(-u\frac{\delta u}{\delta x}\right)_j = -\frac{u_j(-3u_{j+2}+30u_{j+1}+20u_j-60u_{j-1}+15u_{j-2}-2u_{j-3})}{60h}$$

and compare them with the conservative schemes whose coefficients are summarized in Tables II and V. For non-conservative schemes the modified coefficients are simply given by

$$d'_k = -\sum_{l+n=k} k'(l)\hat{u}_l\hat{u}_n \tag{29}$$

and involve the modified wavenumbers of the corresponding scheme for the first derivative; these latter are given by the real part of Equations (39) and (42) in Appendix B. As pointed out in Kravchenko and Moin [5], even when aliasing errors are removed, the conservative and non-conservative schemes are not equivalent. For the central scheme, the discretization errors corresponding to both forms are not very different, as shown in Figure 14. This is no longer true for the upwind scheme, for which a substantial difference clearly appears at low wavenumbers, as shown in Figure 15. In fact, the non-conservative scheme maintains a non-vanishing error along the imaginary axis even when $k \to 0$. This different behavior is explained as follows: for central schemes the modified wavenumber in (29) shows only an odd

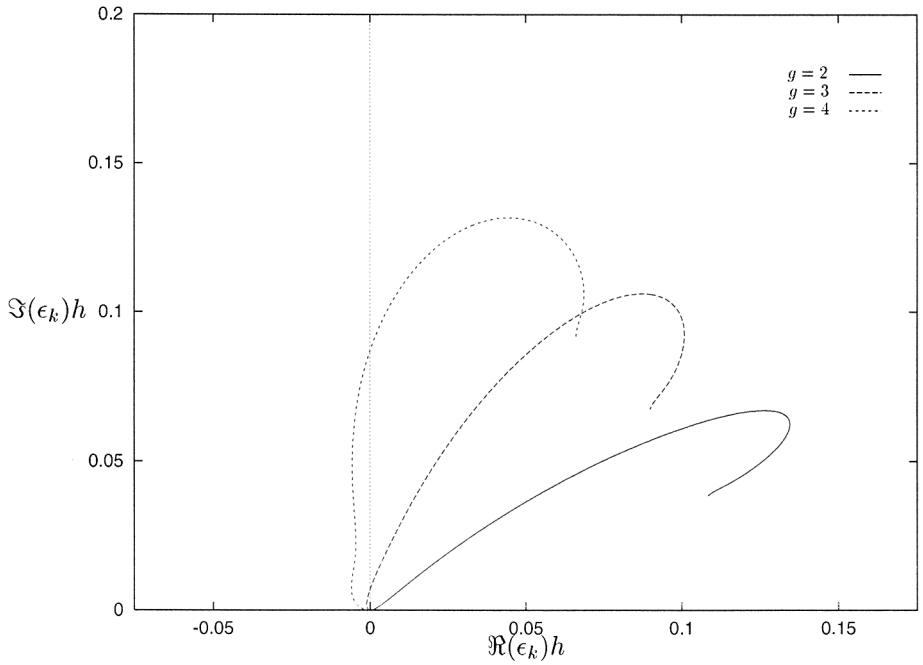

Figure 13. Discretization errors ϵ_k for the upwind scheme, in the absence of de-averaging ($m = 0$) and various interpolation orders. Each point along the curves corresponds to a given value of κ.

Table IV. Coefficients c_{pq} for the fifth-order upwind scheme

c_{pq}	$q=-4$	-3	-2	-1	0	$+1$
$p=-4$	$\frac{1807}{1474560}$	$-\frac{7883}{552960}$	$\frac{14033}{368640}$	$-\frac{14101}{184320}$	$\frac{533}{2211840}$	0
-3		$\frac{11821}{294912}$	$-\frac{22643}{110592}$	$\frac{86801}{221184}$	$\frac{737}{9216}$	$-\frac{533}{2211840}$
-2			$\frac{6013}{24576}$	$-\frac{437}{512}$	$-\frac{103001}{221184}$	$-\frac{71}{20480}$
-1				$\frac{44393}{73728}$	$\frac{143567}{110592}$	$\frac{12967}{368640}$
0					$-\frac{261053}{294912}$	$-\frac{124777}{552960}$
$+1$						$-\frac{1429}{491520}$

real part so that, for small wavenumbers, the corresponding addends in the sum provide a vanishing contribute. On the contrary, for upwind schemes, the modified wavenumber shows also an even imaginary part and the same is no longer true. Finally, one can conclude that

Table V. Coefficients c_{pq} for the fifth-order upwind-biased scheme

c_{pq}	$q=-3$	-2	-1	0	$+1$	$+2$
$p=-3$	$\frac{2941}{4423680}$	$-\frac{4783}{552960}$	$\frac{10313}{368640}$	$\frac{8117}{552960}$	$-\frac{4427}{2211840}$	0
-2		$\frac{24055}{884736}$	$-\frac{18055}{110592}$	$-\frac{29495}{221184}$	$-\frac{31}{27648}$	$\frac{4427}{2211840}$
-1			$\frac{16055}{73720}$	$\frac{3041}{4608}$	$-\frac{11807}{221184}$	$-\frac{833}{61440}$
0				$-\frac{47173}{221184}$	$-\frac{55301}{110592}$	$-\frac{6389}{122880}$
$+1$					$-\frac{27527}{884736}$	$\frac{6643}{552960}$
$+2$						$\frac{1807}{1474560}$

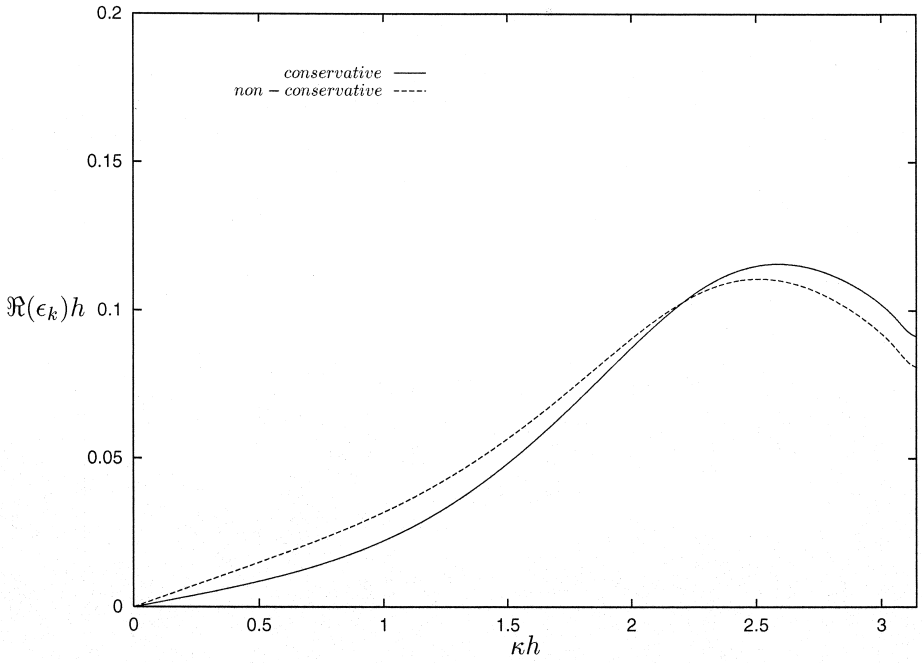

Figure 14. Discretization errors ϵ_k versus grid spacing h, for the fourth-order central scheme in conservative and non-conservative form. In this case, only the real part is involved.

non-conservative upwind schemes are affected by numerical errors at low wavenumbers while the form of the scheme does not significantly affect the spectral distribution of the error at high wavenumbers. This confirms that non-conservative upwind schemes are unsuitable for

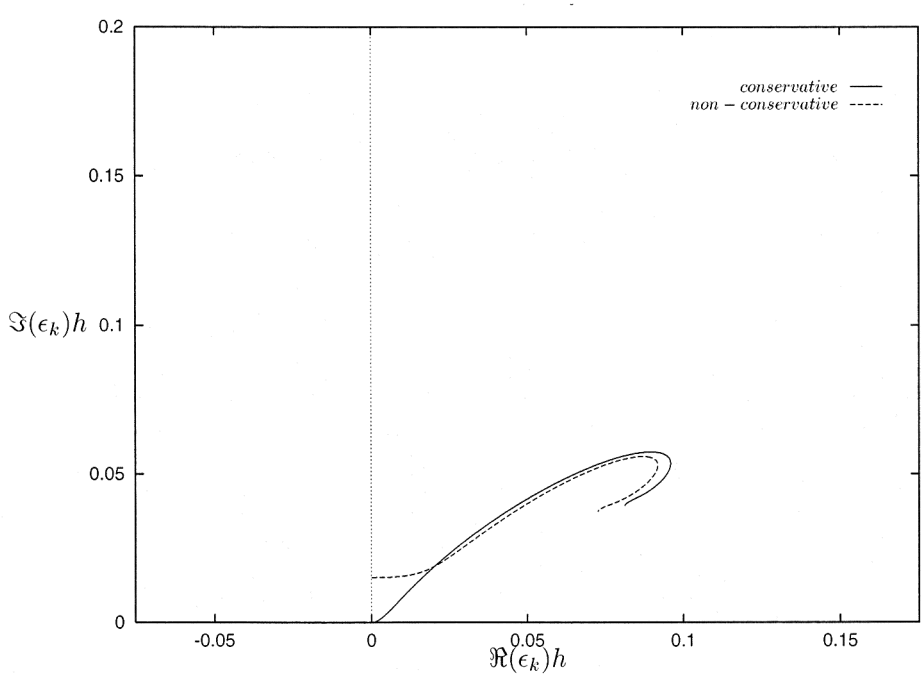

Figure 15. Discretization errors ϵ_k for the fifth-order upwind-biased scheme in conservative and non-conservative form. Each point along the curves corresponds to a given value of κ.

LES of turbulent flows, as also discussed in [16]. On the other hand, the present high-order conservative schemes, consistently set up by means of proper de-averaging and interpolation orders, appear less affected by numerical errors and one can expect their suitability also for LES.

5. A REAL TURBULENT FLOW COMPUTATION

As an application of the present numerical procedure for the simulation of a real turbulent flow, the BFS flow at $Re = 7500$ is considered by adopting a CV approach for the numerical solution of the filtered momentum equations (9) on a structured uniform grid. In order to compute advective and diffusive fluxes at $m = 2$ de-averaging order, we adopt, for each CV boundary, a multi-dimensional second-degree polynomial, defined on a stencil determined according to an upwinding criterion. The multi-dimensional interpolation is necessary because the deconvolution operator to apply on the total flux acts along the three dimensions. By adopting a fractional time step method, the advective fluxes are treated via linearization and the corresponding spatial discretization is a three-dimensional extension of the formula (25).

More details about the numerical procedure can be found in Denaro [6], De Stefano *et al.* [7] and Denaro *et al.* [8].

The effects of the unresolved scales provided by the SGS stress (13) are not explicitly modeled in this application. In fact, the previous analyses showed that the SGS stresses are of rather small relevance in the resolved wavenumber range. Furthermore, as already addressed in Section 2, the high-order filtered ($m > 0$) momentum equation (12) with $\tilde{\tau}_{ik} = 0$ can be interpreted as the top-hat filtered ($m = 0$) equation with the corresponding SGS stress modeled according to a generalized scale-similarity hypothesis [13]. However, in order to prevent energy accumulation at wavenumbers close to the grid cut-off, the implicit dissipation provided by upwind schemes is exploited, too. This is not exactly consistent with the mechanism of physical energy dissipation but it mimics such phenomenon. In fact, the number of grid points we adopt is not sufficient to resolve all the flow scales, especially near the walls, so we let the artificial dissipation of high-order upwind schemes dumping energy pile-up. Nevertheless, as was shown in the previous section, the lower wavenumber components maintain a high accuracy having adopted a conservative formulation. Similar considerations can be found in [29] where in the monotone integrated large eddy simulation (MILES) the dumping of energy at high wavenumbers is provided by the non-linear effects of the flux-corrected transport (FCT) as a built-in SGS model.

5.1. Flow configuration

The simulation concerns the BFS flow at $Re = 7500$, based upon the mean inlet velocity and the full channel height. In order to avoid a strong influence of the outflow conditions, the non-dimensional channel length (x-direction) is assumed to be $L = 10$. The step height (y-direction) is fixed at $h = 0.8$, that corresponds to an expansion ratio of 5:1, while the spanwise width (z-direction) is chosen to be $W = 2$. These extents correspond to a geometry among those considered in Silveira Neto *et al.* [30]. In order to reduce the computational cost, the upstream channel is not considered in the simulation and a uniform velocity profile is assumed as inlet condition at the step edge. Moreover, vanishing normal second derivatives are imposed as outflow conditions. The flow field is assumed to be statistically homogeneous in the spanwise direction, so that periodic boundary conditions are imposed on lateral boundaries, differently from the wall-bounded flow considered in De Stefano *et al.* [7]. Finally, no-slip conditions are considered at normal walls.

The computational domain is discretized by a $101 \times 81 \times 65$ uniform grid. The normal grid resolution close to the walls being rather poor, a grid stretching or a suitable wall law, should be considered (e.g. see [30]). As a matter of fact, the present numerical procedure deals with uniform meshes along each direction, while the formulation in terms of stretched meshes would imply a variable filter width. As it is no longer possible to commute filter operation with differentiation, new metric terms appear in the field equations [18]. In order to make the present formulation suitable for non-uniform meshes, the required modifications are under study and they will be object of future work.

As a first result of the simulation, a normalized re-attachment length $x_r/h \cong 4.5$ is obtained from the analysis of the mean (i.e. spanwise and time averaged) flow. This value is lower than the experimental one [31], depending both on the low resolution in the wall region and on the

adopted uniform inlet velocity profile. In fact, the shape of the latter strongly affects the re-attachment position, as already recognized in De Stefano *et al.* [7]. An instantaneous re-attachment location is defined where the spanwise averaged velocity in the streamwise direction becomes zero at the first grid point away from the wall [32]. In Figure 16 the time evolution of the spanwise averaged re-attachment locations is reported for a time interval containing many shedding periods. The oscillatory evolution is due to the periodical shedding of large spanwise vortices at the step edge.

5.2. Turbulence statistics

In this subsection some low-order statistical results are discussed. When the velocity field has reached a statistically steady state, deduced from the evolution of the solution, the numerical simulation is advanced to set up a time statistical sample. The latter is further increased by averaging over the homogeneous direction, too

$$\langle u_j \rangle(x, y) = \frac{1}{T} \int_{t_0}^{t_0 + T} \mathrm{d}t \, \frac{1}{W} \int_0^W \mathrm{d}z \, u_j(x, y, z, t)$$

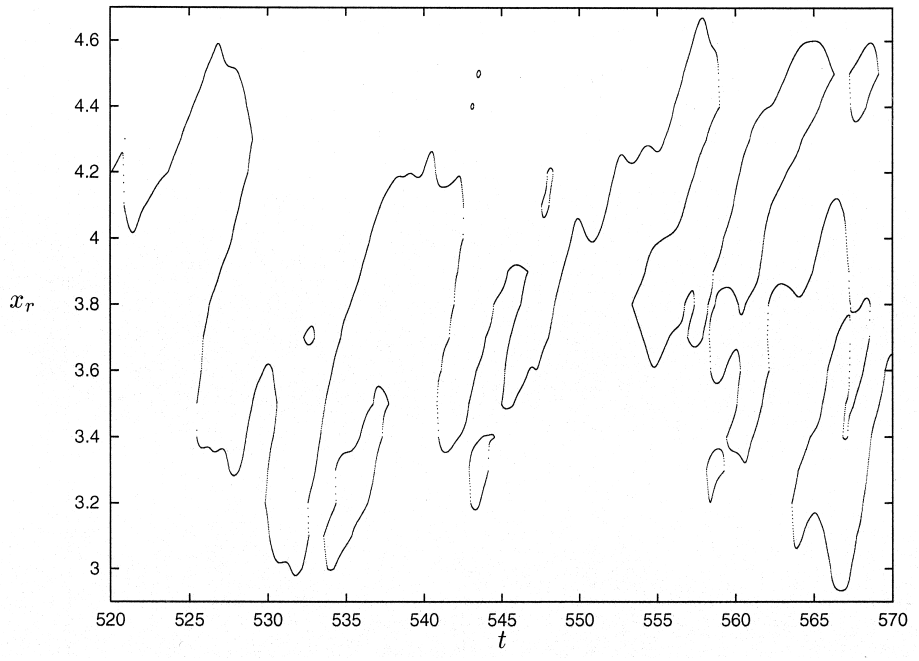

Figure 16. BFS flow: temporal evolution of re-attachment locations for the mean flow.

Time averaging starts at a non-dimensional instant $t_0 \cong 115$ and is pursued over a period $T \cong 400$. The initial instant t_0 is chosen after examining the temporal evolution of the streamwise component.

In order to check the adequacy of the spanwise extent of the computational domain, the two-points spanwise auto-correlations for the three velocity components $R_{u_i u_i}(z)$ are shown in Figure 17 for the position $x = 5$, $y = 0.5$. Spanwise and vertical velocity auto-correlations fall off to zero values for separations of the order of one-half period, while the streamwise component show a small but non-vanishing auto-correlation, differently from [30], therefore a channel width of $W = 2$ does not strictly have a sufficient extent. Nevertheless, the adopted spanwise length seems to be a good compromise between the requirement of a reasonable computational cost and that of a sufficiently large period; in fact, periodical boundary conditions in the homogeneous direction can be adopted only if the computational domain is chosen to capture the large energy containing structures [33]. However, the spanwise grid resolution is adequate, as illustrated in Figure 18, by the one-dimensional energy spectra $E^{(z)}_{u_i' u_i'}(\kappa_z)$ of the three velocity fluctuations $u_i' = u_i - \langle u_i \rangle$, where κ_z stands for the wavenumber in the spanwise direction. Though no SGS modeling has been considered for the deconvolved equations, there is no spurious accumulation of energy at high resolved wavenumbers, where the energy density is some decades lower than at low wavenumbers.

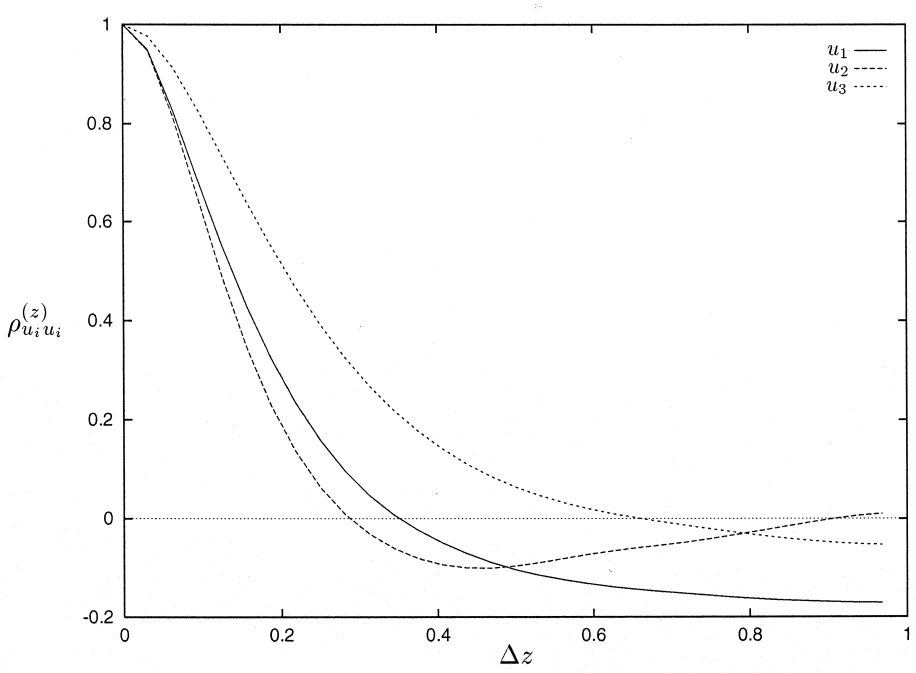

Figure 17. BFS flow: spanwise autocorrelation for the three velocity components, at position $x = 5$, $y = 0.5$.

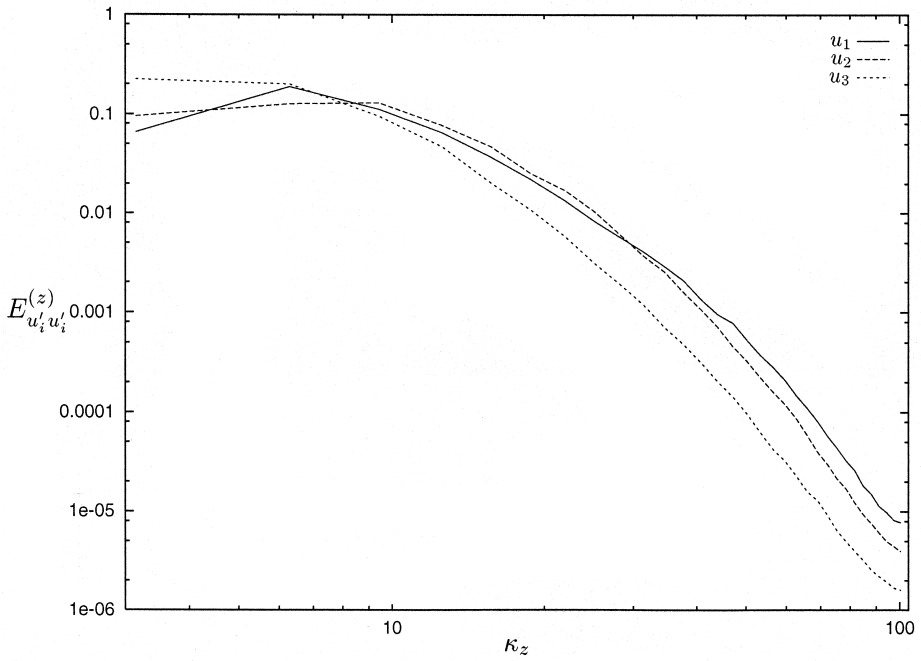

Figure 18. BFS flow: one-dimensional energy spectra in spanwise direction for the three velocity components, at position $x = 5$, $y = 0.5$.

Temporal auto-correlations of the velocity fluctuations are reported in Figure 19 from which it appears that all the velocity components loose their auto-correlation in a short time interval. Frequency energy spectra $E^{(t)}_{u_iu_i}(f)$ are presented in Figure 20, showing a quite flat shape at low wavenumbers, that reflects the presence of a peak in the auto-correlation. Even in this case there is no pile-up of energy at high frequencies, confirming that the adopted numerical scheme provides a certain implicit energy dissipation. It is worth noticing that, while at low frequencies there is a quite clear distinction between the three spectra with the predominance of that corresponding to the streamwise component, at higher ones the energy equally spreads over the different directions, clearly showing a tendency towards isotropy. There is also evidence to some extent of the inertial transfer region at frequencies of unitary order. Finally, in Figure 21 frequency energy spectra of the streamwise component are drawn for three different positions along the channel at $y = 0.5$ and $x = 2.5$, 5, 7.5. The flow topology obviously changes along the channel: the large spanwise structures, present in the region just behind the step, break and eddies of smaller size rise. For increasing distance from the step, high frequency structures appear and energy dissipation occurs, as appears in the figure. The next section provides a qualitative characterization of the flow field.

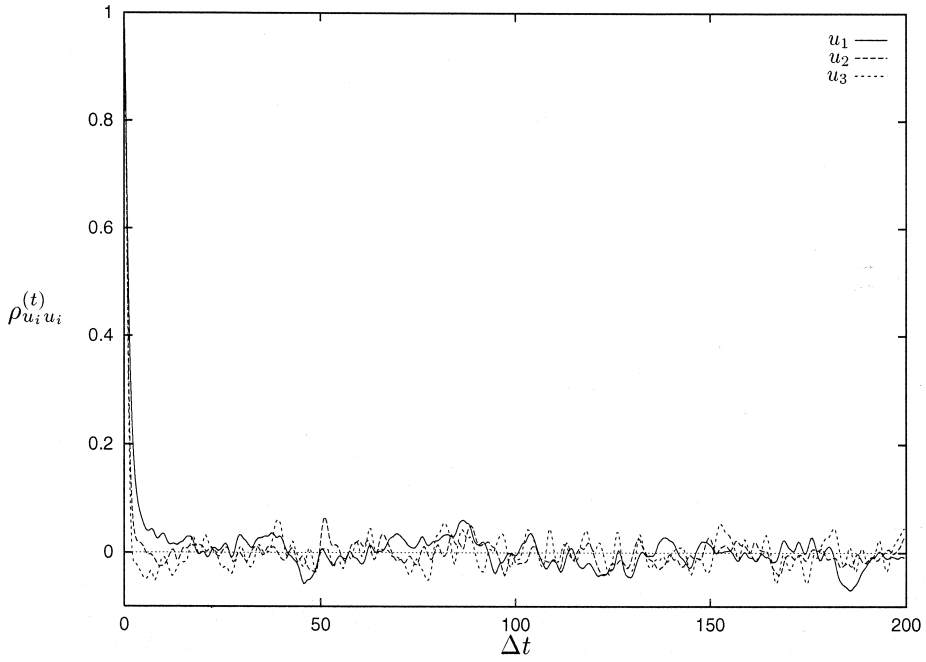

Figure 19. BFS flow: temporal auto-correlations, at position $x = 5$, $y = 0.5$.

5.3. Flow visualization

The numerical visualization of a turbulent flow can be performed by identifying its main vortical structures. Several criteria have been proposed for the identification of these structures, even if a universally accepted definition does not exist yet. Here, the recently proposed definition by Jeong and Hussain [17] is assumed. According to this criterion, a vortex core is a connected region in the flow domain having the second largest eigenvalue, say λ_2, of the symmetric tensor $S_{ik}S_{kj} + \Omega_{ik}\Omega_{kj}$ negative, S_{ij} and Ω_{ij} being the rate-of-strain and the rate-of-rotation tensors respectively.

The structures identified by iso-surfaces at $\lambda_2 = -5$ are shown in Figure 22, where, for the sake of clarity, both three-dimensional (a) and top (b) views are drawn. The choice of zero levels, as the exact application of the definition would require, give more complex pictures, due to the huge amount of detected structures. As a matter of fact, by choosing a relatively small but non-zero level we expect to capture structures of reduced size, i.e. only vortex cores of a certain strength. The vortex reduction has been carried out only in the region just behind the step ($x < 2$), where the large quasi two-dimensional spanwise rolls, generated at the step edge, are broken by the flow. The flow shows a strong three-dimensional character, even just behind the step-edge. In particular, after the breakdown of the large spanwise roll, a large amount of vortical structures appears, most of which elongated in the streamwise direction. It is worth

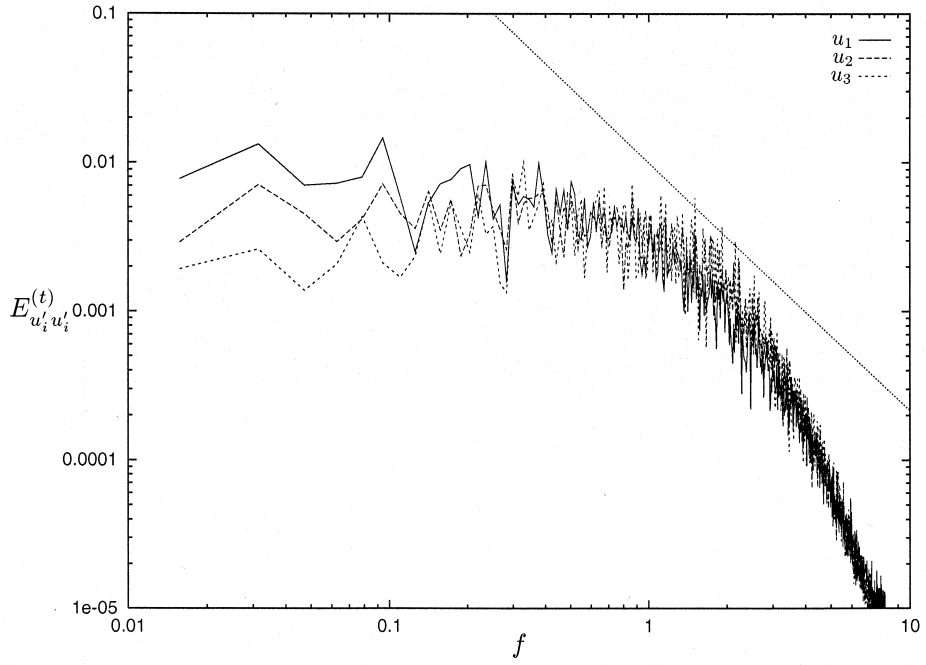

Figure 20. BFS flow: frequency energy spectra, at position $x = 5$, $y = 0.5$.

stressing how the detected structures have been built from the instantaneous flow field and no information can be deduced about their coherence. In order to assess this property, a statistical analysis would be required, as discussed, for example, in Jeong *et al.* [34] for the eduction of coherent wall structures in channel flow.

6. CONCLUDING REMARKS

The CV methods for LES of turbulent flows imply the adoption of the top-hat filter, which does not provide a sharp separation between flow scales. In this paper, we presented a modification of the top-hat filter in order to make it closer to the spectral cut-off one and thus a high-order conservative formulation has been derived. This modification was obtained by means of an approximate deconvolution applied on the top-hat filtered Navier–Stokes equations and a class of high-order filtered evolution equations has been introduced, according to the formal order of the deconvolution. It was shown how the corresponding SGS stress to be modeled becomes less important in the resolved wavenumbers range.

In this framework, the choice of a numerical scheme is extremely delicate: if one requires a better accuracy on the filtered variable, the order of the scheme must be consistently higher and the choice of the stencil appears crucial. In fact, the accuracy analysis for the non-linear

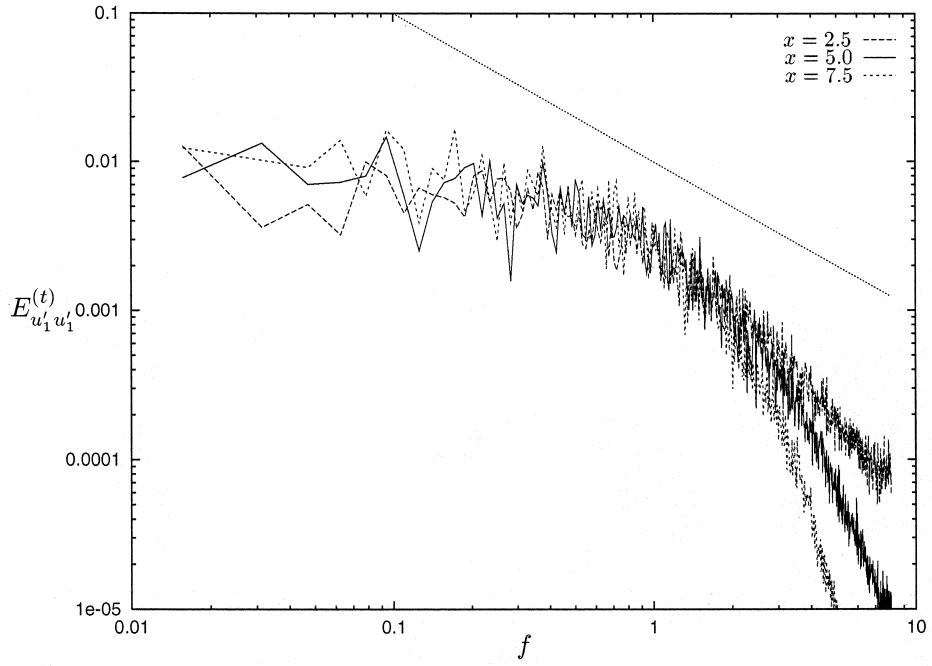

Figure 21. BFS flow: frequency energy spectra for u_1, at positions $x = 2.5,\ 5,\ 7.5,\ y = 0.5$.

one-dimensional transport equation confirmed that central high-order schemes are more suitable for LES based on CV methods, the resolved wavenumbers range not being contaminated by dissipative errors, as happens for non-symmetric stencils. This issue turns out to be fundamental since any SGS model exploits information essentially from the smallest resolved scales, which are those mainly affected by numerical errors. On the other hand, central difference schemes can present stability problems caused by amplification of high frequency solution components, not dumped by numerical dissipation. They are also irrespective of the strong hyperbolic character of high Reynolds number flows, becoming also very sensitive to boundary conditions. Moreover, the adoption of non-uniform grids always implies a non-symmetric stencil. It was shown that fifth-order upwind-biased schemes can result in a good compromise.

The present high-order conservative formulation was tested in a real turbulence case: the flow behind a BFS. The third-order deconvolution was applied on the momentum equation and the corresponding SGS terms were not modeled, but the implicit dissipation provided by the upwind scheme was exploited. Actually, the deconvolved momentum equation without a model for the SGS stresses can be interpreted as the top-hat filtered equation with the corresponding SGS stress modeled according to a generalized scale-similarity hypothesis. In

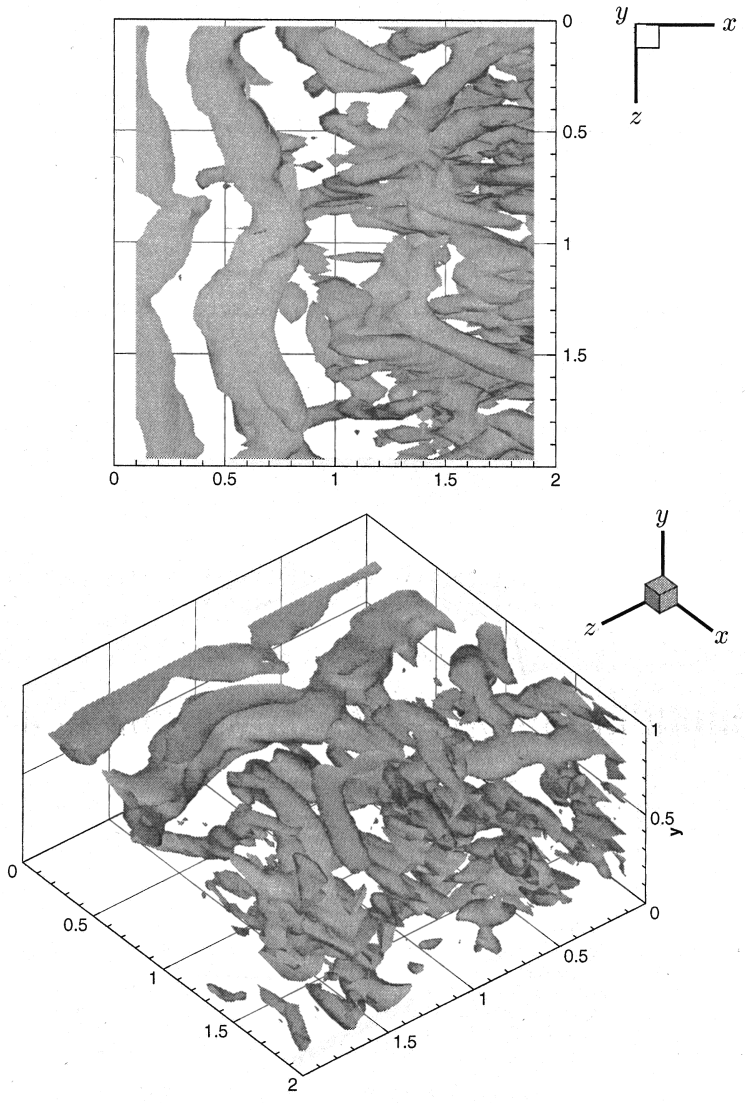

Figure 22. BFS flow: vortical structures bounded by iso-surfaces at $\lambda_2 = -5$.

the future, an SGS model suitable for the high-order filtering will be considered, as well as an extension of the present formulation to non-uniform grids.

APPENDIX A. APPROXIMATE INVERSION OF THE AVERAGING OPERATOR

In this appendix, the existence of the inverse of the operator $I_x - R_x^{(m)}$ is proved and the differential equation (14) is solved to obtain the differential form for the approximate inverse operator $A^{(m)}$. Considered, for an even order $m = 2n$, the differential equation

$$\sum_{p=0}^{n} \frac{(\Delta/2)^{2p}}{(2p+1)!} g^{(2p)}(x) = f(x) \tag{30}$$

in which $f(x) = \bar{g}(x)$, the associated homogeneous problem has only the trivial solution. In fact, for $f \equiv 0$, it follows $0 \equiv f'(x) \propto g(x + \Delta/2) - g(x - \Delta/2)$, i.e. the solution γ of the homogeneous problem is a periodic function with period Δ. Its Fourier series, by assuming $\kappa = k2\pi/\Delta$, follows

$$\gamma(x) = \sum_k \gamma_k \, \mathrm{e}^{\mathrm{i}\kappa x} \tag{31}$$

with

$$\gamma_k = \frac{1}{\Delta} \int_{-\Delta/2}^{\Delta/2} \mathrm{d}x \, \gamma(x) \, \mathrm{e}^{-\mathrm{i}\kappa x}$$

and $\gamma_0 = 0$. By substituting (31) into (30), one obtains

$$\sum_k \gamma_k a_k \, \mathrm{e}^{\mathrm{i}\kappa x} \equiv 0 \tag{32}$$

with the coefficients

$$a_k = a_{-k} = \sum_{p=0}^{n} \frac{(-1)^p}{(2p+1)!} (\pi k)^{2p}$$

Finally, with $a_k \neq 0$ for all $k \neq 0$, Equation (32) provides $\gamma_k = 0$.

Concerning the approximate inverse operator, a differential expression can be deduced in the hypothesis that $\tilde{u}(x) \, \mathrm{e}^{-\beta x} \to 0$ for $x \to -\infty$ and for all $\beta > 0$. The solution of Equation (14) is given by

$$\tilde{u}(x) = \sum_{l=1}^{m} b_l \int_{-\infty}^{x} \mathrm{d}\xi \, \mathrm{e}^{\alpha_l (x-\xi)} \, \bar{u}(\xi) \tag{33}$$

where the coefficients b_l are defined by

$$b_l = (-1)^l \frac{(m+1)!}{(\Delta/2)^m} \frac{V(\alpha_l, \ldots, \alpha_{l-1}, \alpha_{l+1}, \ldots, \alpha_m)}{V(\alpha_1, \ldots, \alpha_m)}$$

in which α_i $(i=1,\ldots,m)$ are the roots of the characteristic equation associated to (30) and V is a Vandermonde determinant. By means of repeated integration by parts, the following expression holds

$$\mathrm{e}^{\alpha_l x}\int_{-\infty}^{x}\mathrm{d}\xi\ \mathrm{e}^{-\alpha_l\xi}\,\bar{u}(\xi)=-\sum_{p=1}^{6}\frac{\bar{u}^{(p-1)}(x)}{\alpha_l^p}+\frac{\mathrm{e}^{\alpha_l x}}{\alpha_l^6}\int_{-\infty}^{x}\mathrm{d}\xi\ \mathrm{e}^{-\alpha_l\xi}\,\bar{u}^{(6)}(\xi)$$

and by inserting it into Equation (33), $\tilde{u}$ is given by

$$\tilde{u}(x)=\sum_{p=1}^{6}\left(-\sum_{l=1}^{2n}\frac{b_l}{\alpha_l^p}\right)\bar{u}^{(p-1)}(x)+\cdots \tag{34}$$

The sum $-\Sigma_{l=1}^{2n}\,b_l/\alpha_l^p$, apart from the factor $-(2/\Delta)^{2n}(2n+1)!/V(\alpha_1,\ldots,\alpha_{2n})$, represents the expansion with respect to the last row of the determinant

$$|\mathscr{M}_p|\equiv\begin{vmatrix}1 & 1 & \ldots & 1\\ \alpha_1 & \alpha_2 & \ldots & \alpha_{2n}\\ \alpha_1^2 & \alpha_2^2 & \ldots & \alpha_{2n}^2\\ \vdots & \vdots & & \vdots\\ \alpha_1^{2n-2} & \alpha_2^{2n-2} & \ldots & \alpha_{2n}^{2n-2}\\ \alpha_1^{-p} & \alpha_2^{-p} & \ldots & \alpha_{2n}^{-p}\end{vmatrix}$$

that holds $-V(\alpha_1,\ldots,\alpha_{2n})/(\alpha_1\ldots\alpha_{2n})$ for $p=1$, as it can be proved by combining its rows. In the same way, for $p>1$, it can be expressed as

$$|\mathscr{M}_p|=-\frac{V(\alpha_1,\ldots,\alpha_{2n})}{\alpha_1\ldots\alpha_{2n}}\sum_{(r_1,\ldots,r_{p-1})}^{(1,\ldots,2n)}\frac{1}{\alpha_{r_1}\ldots\alpha_{r_{p-1}}}$$

where the sum, indicated with $\Sigma_{p-1}(\alpha_1^{-1},\ldots,\alpha_{2n}^{-1})$ in the following, extends over all possible combinations of the $p-1$ integers $r_1,\ldots,r_{p-1}$ ranging from 1 to $2n$ and the indexes $r_1,\ldots,r_{p-1}$ are not necessarily different. It may be calculated by exploiting the coefficients in Equation (30).

The odd derivatives of u being absent, the sum

$$S_q(\alpha_1,\ldots,\alpha_{2n})=\sum_{(p_1,\ldots,p_q)}^{(1,\ldots,2n)}\alpha_{p_1}\ldots\alpha_{p_q}$$

of all possible products of q different roots vanish for odd q. For the sake of simplicity, we call the sum herein appearing $S_q(\alpha_1,\ldots,\alpha_{2n})$, to distinguish it from $\Sigma_{p-1}(\alpha_1^{-1},\ldots,\alpha_{2n}^{-1})$. In particular, by normalizing the coefficients in (30) with respect to the one of the derivative of order $2n$, it results

$$S_{2n}(\alpha_1, \ldots, \alpha_{2n}) = \alpha_1 \ldots \alpha_{2n} = \frac{(2n+1)!}{(\Delta/2)^{2n}} \tag{35}$$

from which it follows that the coefficient of $\bar{u}$ (i.e. $-\Sigma_{l=1}^{m} b_l/\alpha_l$) is equal to 1 and the coefficient of $\bar{u}^{(p-1)}$, for $p>1$, $(-\Sigma_{l=1}^{m} b_l/\alpha_l^p)$ is given by Σ_{p-1}.

The coefficient of $\bar{u}^{(1)}$ $(p=2)$ in Equation (34) is Σ_1, which vanishes as $S_{2n-1}=0$. The coefficient of $\bar{u}^{(2)}$ $(p=3)$ is Σ_2 and it is given, according to Equation (35), by

$$C_2 = -\frac{S_{2n-2}}{\alpha_1 \ldots \alpha_{2n}} = -\frac{\Delta^2}{24} \tag{36}$$

The coefficient of $\bar{u}^{(3)}$ $(p=4)$ is Σ_3, which vanishes as $S_{2n-3}=0$. As a matter of fact, from the absence of odd derivatives in Equation (30), the same occurs for the coefficients of each term of odd order, so that the differential from of the inverse operator contains only derivatives of even order. It remains to evaluate the coefficient of $\bar{u}^{(4)}$ $(p=5)$, which is given by Σ_4

$$C_4 = S_2^2 - S_4 = \left(\frac{\Delta^2}{2^2 3!}\right)^2 - \frac{\Delta^4}{2^4 5!} = \frac{7}{5760}\Delta^4 \tag{37}$$

Analogously, it is possible to deduce the coefficient of higher order.

The inverse operator is finally written up to terms of order Δ^6 as

$$A_x^{(5)} = I_x + C_2 \frac{\mathrm{d}^2}{\mathrm{d}x^2} + C_4 \frac{\mathrm{d}^4}{\mathrm{d}x^4} \tag{38}$$

with the definitions (36) and (37) of the coefficients C_2 and C_4.

APPENDIX B. MODIFIED WAVENUMBERS FOR UPWIND SCHEMES

Each FD scheme for the evaluation of a numerical first derivative can be conveniently examined in Fourier space in terms of its modified wavenumber [15]. In this appendix the modified wavenumbers for the upwind schemes considered in the text are reported:

- third-order

$$\kappa' = \frac{\sin(\kappa h)[4-\cos(\kappa h)]}{3h} + \mathrm{i}\,\frac{-2+4\cos(\kappa h)-2\cos^2(\kappa h)}{6h} \tag{39}$$

- fourth-order

$$\kappa' = \frac{\sin(\kappa h)[5-3\cos(\kappa h)+\cos^2(\kappa h)]}{3h} + \mathrm{i}\,\frac{-1+3\cos(\kappa h)-3\cos^2(\kappa h)+\cos^3(\kappa h)}{3h} \tag{40}$$

- fifth-order

$$\kappa' = \frac{\sin(\kappa h)[28 - 27\cos(\kappa h) + 20\cos^2(\kappa h) - 6\cos^3(\kappa h)]}{15h} + \mathrm{i}\,\frac{-2 + 12\cos(\kappa h) - 24\cos^2(\kappa h) + 20\cos^3(\kappa h) - 6\cos^4(\kappa h)}{15h} \tag{41}$$

- fifth-order biased

$$\kappa' = \frac{\sin(\kappa h)[22 - 9\cos(\kappa h) + 2\cos^2(\kappa h)]}{15h} + \mathrm{i}\,\frac{-2 + 6\cos(\kappa h) - 6\cos^2(\kappa h) + 2\cos^3(\kappa h)}{15h} \tag{42}$$

Plots of real and imaginary parts of these modified wavenumbers are reported in Figure 6. It is worth stressing that real parts are odd functions, as it happens for central schemes, whilst those imaginary ones are even. Moreover, for a given odd order of accuracy, the real part of the modified wavenumber for an upwind scheme coincides with the one of the central scheme of the next order (for example, the real part of Equation (39) corresponds also to the fourth-order central FD scheme). Naturally, the limit

$$\lim_{\kappa h \to 0} \frac{\kappa'}{\kappa} = 1, \tag{43}$$

ensures the consistency of the schemes.

REFERENCES

1. Deardorff JW. A numerical study of three-dimensional turbulent flow at large Reynolds numbers. *Journal of Fluid Mechanics* 1970; **41**: 453–480.
2. Schumann U. Subgrid scale model for finite difference simulations of turbulent flows in plane channels and annuli. *Journal of Computational Physics* 1975; **18**: 376–404.
3. Lund TS, Kaltenbach HJ. Experiments with explicit filtering for LES using a finite-difference method. *CTR Annual Research Briefs* 1995: 91–105.
4. Ghosal S. An analysis of numerical errors in large eddy simulation of turbulence. *Journal of Computational Physics* 1996; **125**: 187–206.
5. Kravchenko AG, Moin P. On the effect of numerical errors in large eddy simulation of turbulent flows. *Journal of Computational Physics* 1997; **131**: 310–322.
6. Denaro FM. Towards a new model-free simulation of high-Reynolds flows: local average direct numerical simulation. *International Journal for Numerical Methods in Fluids* 1996; **23**: 125–142.
7. De Stefano G, Denaro FM, Riccardi G. Analysis of 3D backward-facing step incompressible flow via a local average-based numerical procedure. *International Journal for Numerical Methods in Fluids* 1998; **28**: 1073–1091.
8. Denaro FM, De Stefano G, Riccardi G. Local-average based numerical simulation of turbulent flows. In *Advances in DNS/LES*, Liu C, Liu Z (eds). Greyden Press: Columbus, 1997; 273–280.
9. Vasilyev OV, Lund TS, Moin P. A general class of commutative filters for LES in complex geometries. *Journal of Computational Physics* 1998; **146**: 105–123.

10. Leonard A. Energy cascade in large eddy simulation of turbulent fluid flow. *Advances in Geophysics* 1974; **18**(A): 237–248.
11. Shah KB, Ferziger JH. A new non-eddy viscosity subgrid-scale model and its application to channel flow. *CTR Annual Research Briefs* 1995: 73–90.
12. Geurts BJ. Inverse modeling for large eddy simulation. *Physics of Fluids* 1997; **9**(12): 3585–3587.
13. Stolz S, Adams NA. An approximate deconvolution procedure for large-eddy simulation. *Physics of Fluids* 1999; **11**(7): 1699–1701.
14. Kuerten JMG, Geurts BJ, Vreman AW, Germano M. Dynamic inverse modeling and its testing in large-eddy simulations of the mixing layer. *Physics of Fluids* 1999; **11**(12): 3778–3785.
15. Ferziger JH, Perić M. *Computational Methods for Fluid Dynamics*. Springer: Berlin, 1996.
16. Mittal R, Moin P. Suitability of upwind-biased finite difference schemes for large-eddy simulation of turbulent flows. *AIAA Journal* 1997; **35**(8): 1415–1417.
17. Jeong J, Hussain F. On the identification of a vortex. *Journal of Fluid Mechanics* 1995; **285**: 69–94.
18. Ghosal S, Moin P. The basic equations for the large eddy simulation of turbulent flows in complex geometry. *Journal of Computational Physics* 1995; **118**: 24–37.
19. Kim J, Moin P. Applications of a fractional step method to incompressible Navier–Stokes equations. *Journal of Computational Physics* 1985; **59**: 308–323.
20. Harten A, Osher S. Uniformly high order accurate essentially non-oscillatory schemes. *SIAM Journal of Numerical Analysis* 1987; **24**: 279–309.
21. Grasso F, Meola C. Euler and Navier–Stokes equations for compressible flows: finite-volume methods. In *Handbook of Computational Fluid Mechanics*, Peyret R (ed.). Academic Press: London, 1996; 159–282.
22. Love MD. Subgrid modelling studies with Burgers' equation. *Journal of Fluid Mechanics* 1980; **100**: 87–110.
23. Bardina J, Ferziger JH, Reynolds WC. Improved subgrid models for large-eddy simulation. AIAA Paper 80-1357, 1980.
24. Rogallo RS, Moin P. Numerical simulation of turbulent flows. *Annual Review of Fluid Mechanics* 1984; **16**: 99–137.
25. Collatz L. *The Numerical Treatment of Differential Equations*. Springer: Berlin, 1966.
26. Rai MM, Moin P. Direct simulations of turbulent flow using finite-difference schemes. *Journal of Computational Physics* 1991; **96**: 15–53.
27. Rai MM, Moin P. Direct numerical simulation of transition and turbulence in a spatially evolving boundary layer. *Journal of Computational Physics* 1993; **109**: 169–192.
28. Morinishi Y, Lund TS, Vasilyev OV, Moin P. Fully conservative higher order finite differences schemes for incompressible flows. *Journal of Computational Physics* 1998; **143**: 90–124.
29. Boris JP, Grinstein FF, Oran ES, Kolbe RL. New insights into large eddy simulation. *Fluid Dynamics Research* 1992; **10**: 199–228.
30. Silveira Neto A, Grand D, Mètais O, Lesieur M. A numerical investigation of coherent vortices in turbulence behind a backward-facing step. *Journal of Fluid Mechanics* 1993; **256**: 1–25.
31. Armaly BF, Durst F, Pereira JCF, Schonung B. Experimental and theoretical investigation of backward-facing step flow. *Journal of Fluid Mechanics* 1983; **127**: 473–486.
32. Le H, Moin P, Kim J. Direct numerical simulation of turbulent flow over a backward-facing step. *Journal of Fluid Mechanics* 1997; **330**: 349–374.
33. Kim J, Moin P, Moser R. Turbulence statistics in fully developed channel flow at low Reynolds number. *Journal of Fluid Mechanics* 1987; **177**: 133–166.
34. Jeong J, Hussain F, Schoppa W, Kim J. Coherent structures near the wall in a turbulent channel flow. *Journal of Fluid Mechanics* 1997; **332**: 185–214.

